ISSN 09731784

Journal of Dynamics of Fluids

Volume No. 13

Issue No. 2

May - August 2025

ENRICHED PUBLICATIONS PVT.LTD

JE - 18,Gupta Colony, Khirki Extn,
Malviya Nagar, New Delhi - 110017.
E- Mail: info@enrichedpublication.com
Phone :- +91-8877340707

ISSN 09731784

Journal of Dynamics of Fluids

Aims and Scope

Journal of Dynamics of fluids is an scientific journal that publishes articles, research notes, debate and short reports in all areas of Fluid Dynamics.

Subject areas suitable for publication include, but are not limited to the following fields:

- Aeroacoustics
- Bluff Body Flows
- Bubbles and Droplets
- Dynamics of Dispersed Particles
- Fluid-structure Interactions
- Flow Stability and Transition to Chaos
- Flow Control Methods
- Gravitational Convection Solidification

ISSN 09731784

Journal of Dynamics of Fluids

ISSN 09731784

Journal of Dynamics of Fluids

(Volume No. 13, Issue No. 2, May - August 2025)

Contents

ISSN 09731784

Finite Difference Modeling On The Temperature Field Of Consumable-Rod And Substrate In Friction Surfacing Process

V. Pitchi Raju*1 and M. Manzoor Hussain 2

1* Associate Professor in Mechanical Engineering Dept, Princeton College of Engg. & Tech, Hyderabad, 2 Professor in Mechanical Engineering Dept, J. N. T. University, Hyderabad, India.

ABSTRACT

Friction surfacing is a solid state coating process with applications of wear and corrosion resistance coatings and also used for reclamation and repair of damaged and worn components. Friction surfacing is a kind of thermal processing technology, in which the temperature profile obtained and changes of temperature occurred in consumable rod and substrate are significant factors to obtain high quality of coatings. In the present work, the temperature fields of the consumable rod and substrate during the process are simulated by finite difference modeling method, And also heat source model of the consumable rod and substrate are established in friction surfacing process. The obtained results are consistence with experimental values. Reoccurring of the changes of temperature of both consumable rod and substrate while conducting friction surfacing process, hence furnishing theoretical information for the selection of primary technical factors in industrial engineering applications and which permits additional work for producing quality of coatings in friction surfacing process.

Keywords: *Friction surfacing, Temperature field, consumable rod, substrate, finite difference modeling*

1. INTRODUCTION

Friction surfacing is an emerging surface modification technique, which is derived from the friction welding process. In this process, a rotating consumable rod is fed against substrate with certain axial pressure, and then frictional heat is produced between the consumable rod and substrate. As soon as the rubbing end of the rotating consumable rod is get plasticized, the substrate start moves horizontally relative to vertical consumable rod, then plasticized metal being deposited as a coating over the substrate, the Friction surfacing process has been adopted for getting several hard metal coatings such as tool steel coatings over low carbon steel. The frictional heating between tip of consumable rod and substrate caused to the formation of a heat affected zone nearer to the interface of the consumable rod and substrate. However this heat affected zone is lesser compared to that generated by welding [1]. The friction surfacing process has a several advantages such as zero dilution, clean, dense and fine microstructure, no cracking in the heat affected(HAZ), excellent bonding with absence of porosity, inclusions or oxidation over the conventional welding processes [2].

Presently many researchers have been concentrated about this process particularly on its technical parameters due to its engineering background. The frictional heat is passing along the consumable rod, creating a temperature difference that evaluates the amount deformation [3]. The consumable rod material gradually gets softened and plastic deformation by temperature gradient in a compression/torsion process through colder material [4]. Moreover, the material is transferred through rotational contact plane across which slippage take place between the deposited layer and consumable rod [5]. From the previous studies, it is revealed that to speed up the selection of process parameters by development of neurofuzzy model based Decision support system [6, 7, 8]. The calculation of process parameters are based on mathematical modeling in friction surfacing regimes [9]. And also attempts made onto identify the feasibility of different types of consumable rod materials (aluminum, stainless steel and brass) over substrates under different environmental conditions [10]. The study of interfacial phenomena of different materials (mild steel with tool steel and inconel [11] and aluminum with steel [12] during friction surfacing process.

Though most of the studies focus on ferrous alloys, there are few investigations with non-ferrous alloys like aluminum. It was investigated on both single and multilayering by AA 2017 alloy deposited over AA 5052 substrates [13]. The recent studies performed on the grain refinement process of an AA 6082-T6 coating over AA 2024-T3 substrate and also found that shear deformation is the main cause of recrystallization and grain deformation in friction surfacing process [14].

Besides the studies on technical characteristics, more studies focus on identifying the process mechanism. The discussion on mechanism of auto-hardening of the coating layer [15] and also on concept of real rotational contact plane in friction surfacing [5]. The optimization of process parameters and process modeling were investigated for various material combinations [8], which build the feasibility of producing several alloy steel coatings for wear and corrosion resistance coatings. And also the selection of process parameters in applications of friction surfacing is performed by using intelligent decision support [6].

In the present study, the finite difference modeling method was used to simulate the consumable rod's and substrate's temperature field. The temperature field in this process, particularly of the consumable rod and substrate is observed as a crucial element in the selection of process parameters and process mechanism. The results of this investigation can furnish theoretical guidance selection of process parameters and analyzing the feasibility.

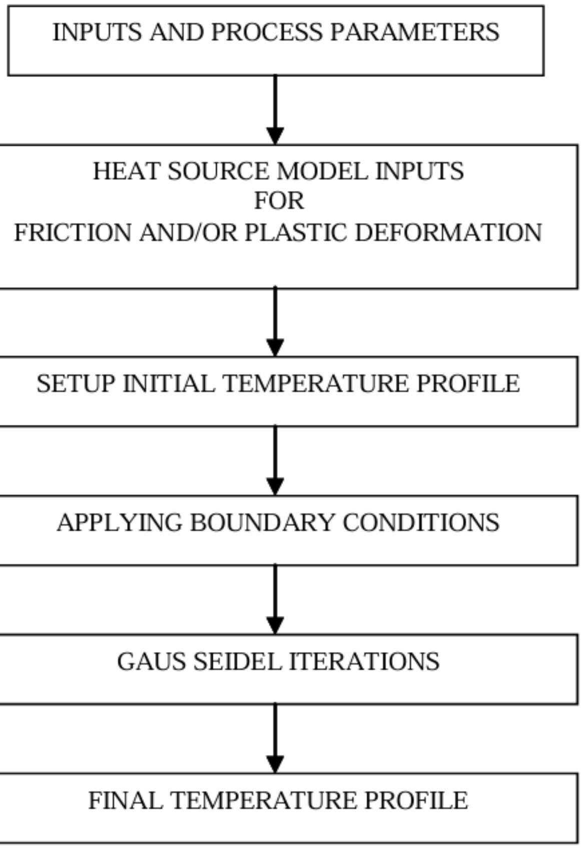

Figure 1: Flow chart for mathematical modeling

2. HEAT SOURCE MODEL IN CONSUMABLE ROD

The total friction surfacing process is divided into two consequent phases i. e. the preliminary friction preheating phase and later steady friction surfacing phase. At the starting of the process, heat generated due to friction is considered as main heat source. When the temperature enhances, local regions at the tip of the rod is plasticized primarily by the friction heat and shear forces. Hence heat due to plastic deformation becomes the primary heat source. The process is executed on as the plasticized local regions at the tip of the rod constantly increase up to total interface turns to plasticized. At the end of the initial friction preheating phase, the main heat source converted from friction heat source to plastic deformation heat source.

The heat liberated by friction is adequate to generate a hot plasticized zone, in fact, at the end of the initial friction preheating phase, the temperature field of the consumable rod's starts to get a quasi-steady condition. In the later friction surfacing phase, the temperature field maintains its quasi-steady status throughout the process. Hence, the attention is focus on this study primarily on calculating the temperature field in the preheating phase [16].

2.1 Friction Heat Source Model in Consumable Rod

In friction surfacing process, while preheating phase, the heat is generated primarily due to friction between the rubbing end of the consumable rod and substrate, depends on the assumption that distribution of force remains constant, friction heat was executed by following sequential steps.

Initially, an annulus with an inner radius of r and width of dr at the friction interface was generated as shown in fig 1.

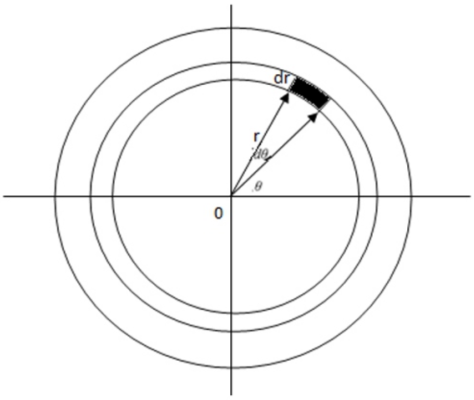

Figure 2: Element at Friction Interface

2.2 Plastic Stage Deformation Heat Source Model

The total plastic deformation heat power qv can be divided into two parts i. e. the deformation heat power of the circumferential shear qs and the deformation heat power of the axial direction compressing qa. Thus, it is very easy to calculate the total plastic deformation heat power, when the two parts are available. The axial force, surfacing time and axial reduction length of the consumable rod can be used for calculating the plastic deformation heat power of axial compressing. The deformation heat power of the circumferential shear can be computed through the time of the surfacing layer and figuration size. The axial reduction length of the consumable –rod in surfacing td and volume of the plastic metal is Δ V [16].

2.3 Simulation Results and Discussion

The consumable rod material tool steel M2 consists of following physical characteristics: mass density ρ1= 8160 Kg/m3, thermal conductivity λ1= 0. 024 W/ m k, specific heat capacity c1 = 460 J/Kg K, and melting temperature Tm = 4680 0 C, the substrate material is low carbon steel with following physical characteristic: mass density ρ2= 7856 Kg/m3, thermal conductivity λ2 = 0. 054 W/ m k, and specific heat capacity c2 = 490 J/Kg K, The diameter of the consumable rod is 10. 5 mm, and the surfacing force is 5 and 10 KN conducted separately, and the rotating speed is 100 and 300 rpm respectively. The friction coefficient between consumable-rod and substrate is 0. 8. Fig 4. Shows the simulation result of temperature of the consumable rod at friction interface.

Table 1: Pre-heating time related to process parameter.

S. No	surfacing force (MPa or N/mm$^{2)}$	Rotating speed (RPM)	Preheating time (Sec)
1	5	100	15. 5
2	5	300	15. 0
3	10	100	9. 7
4	10	300	9. 0

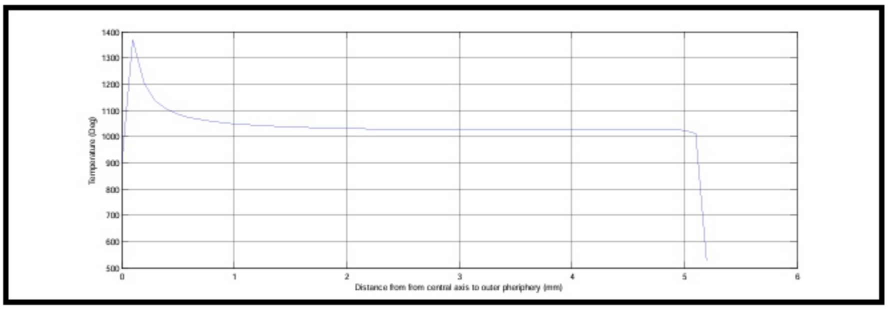

Figure 3: Temperature gradient from central axis towards outer periphery at friction interface

Besides these simulation results, the simulation program can give guidance in deciding friction preheating time for various feasible material combinations.

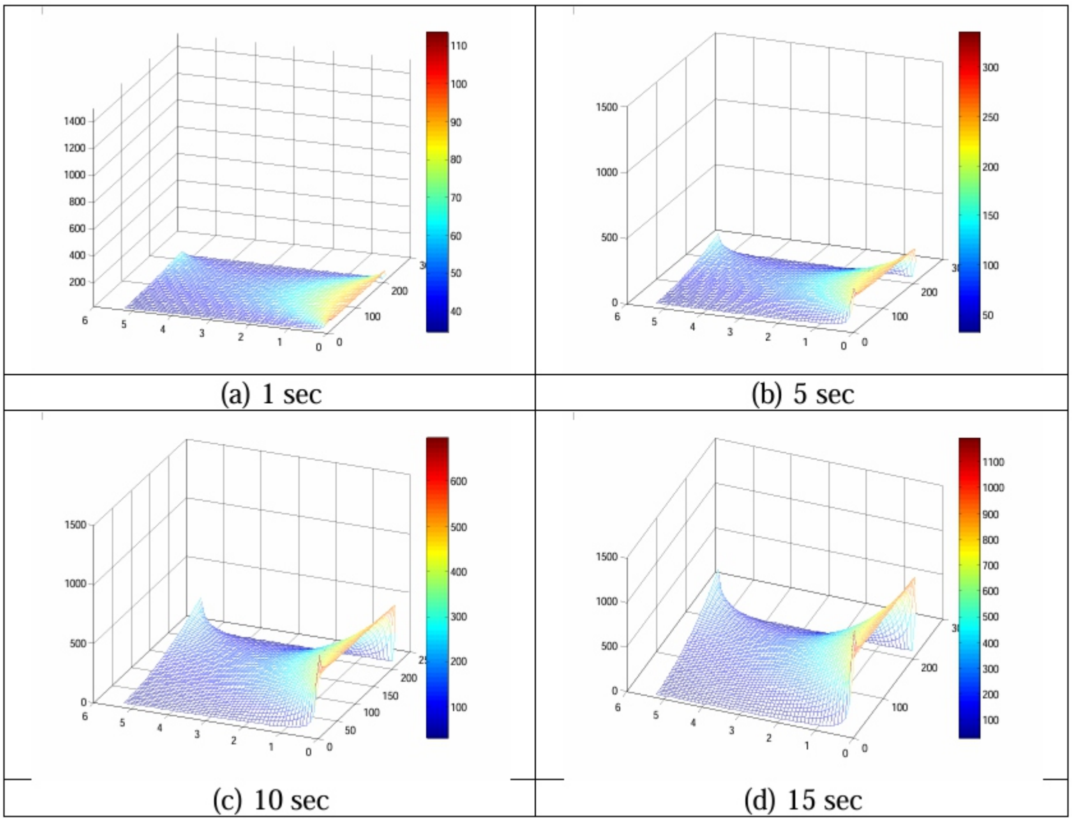

(a) 1 sec

(b) 5 sec

(c) 10 sec

(d) 15 sec

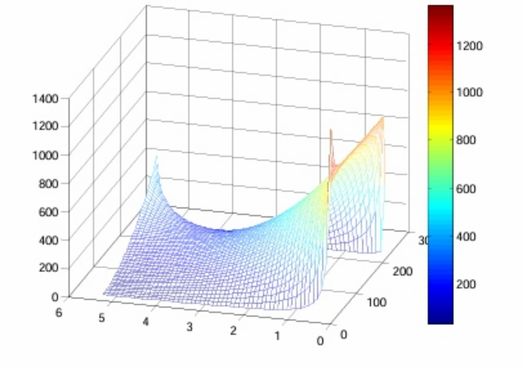

(e) 15. 5 sec

Figure 4: Temperature profile at the center section of the consumable rod at various timings (P = 5 MPa ; N = 100 RPM; td = 5 mm)

3. HEAT SOURCE MODEL IN SUBSTRATE

Generally total friction surfacing process can be divided into two successive phases I. e. preliminary friction preheating phase and later steady surfacing phase. At the starting of the friction surfacing process, friction heat is the primary heat source. In friction surfacing process, the friction interface is initially at lower end of the consumable-rod, after the process obtains steady state, the friction interface transfer to the coating layer position. Whereas the friction interface is noticed as at the substrate in exact position. The substrate thickness is d, and coating layer thickness is h, thus if the substrate thickness is designated to be (h/2 + d), then the process will be simplified more, the heat source model of substrate alters to the transient local transfer heat flux over a substrate of (h/2 + d) thick [17], as shown in fig 5.

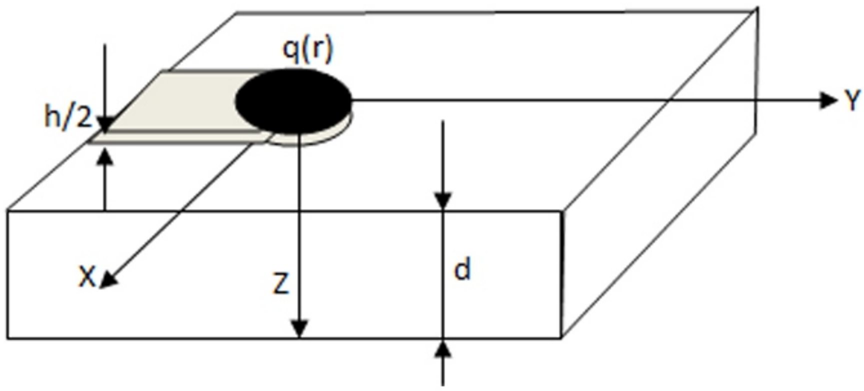

Figure 5: The heat transfer model of substrate

The exchange of heat between the substrate and surrounding environment related to the third classes, as shown below.

$$-\lambda \frac{\partial T}{\partial n} = \alpha(T - T_f) \tag{1}$$

Where convection heat exchange coefficient is α, outer atmosphere temperature is T_f. The selection of moving coordinate (X, Y, Z) with respect to origin o is illustrated in fig 2. Then the heat transfer differential becomes as

$$\rho c.\left(\frac{\partial T}{\partial t} + \nu.\nabla T\right) = \nabla.(\lambda \nabla T) + q_v + \phi \tag{2}$$

Where ν, ρ, ∇, c, q_v, λ and Φ represents moving velocity of the substrate, mass density, nabla operator, specific heat capacity, inner heat source, heat exchange coefficient and dissipation function respectively.

Whereas in solid state heat exchange, Φ=0, q_v = 0, and only velocity remains exists, hence the moving coordinate can be moved to the static coordinate, and the following can be obtained.

$$\frac{\partial^2 T}{\partial x^2} + \frac{\partial^2 T}{\partial Y^2} + \frac{\partial^2 T}{\partial z^2} = \left(\frac{1}{a}\right)\frac{\partial T}{\partial t} - \left(\frac{v}{a}\right)\frac{\partial T}{\partial Y} \tag{3}$$

Due to property of symmetry, only half portion of the substrate is measured [17].

3.1 SIMULATION RESULTS OF THE SUBSTRATE

The substrate material low carbon steel consists of following characteristics: thermal conductivity λ = 0. 054 W/ m k, mass density ρ =7856 Kg/m3, specific heat capacity c = 460 J/Kg K, melting temperature Tm = 1400 0 C, the dimension of the substrate: 310 mm x 220 mm x 11 mm, The surfacing force is 5 MPa, the rotating speed is 100 rpm, the friction coefficient between substrate and consumable-rod is selected as 0. 8. The moving speed of the substrate is 40 mm /min. for the selected process parameters, the preheating time is 15. 5 seconds. The temperature field of the friction system attains stable after 15. 5 seconds. The simulation results of the substrate as illustrated in fig 6. to fig 10.

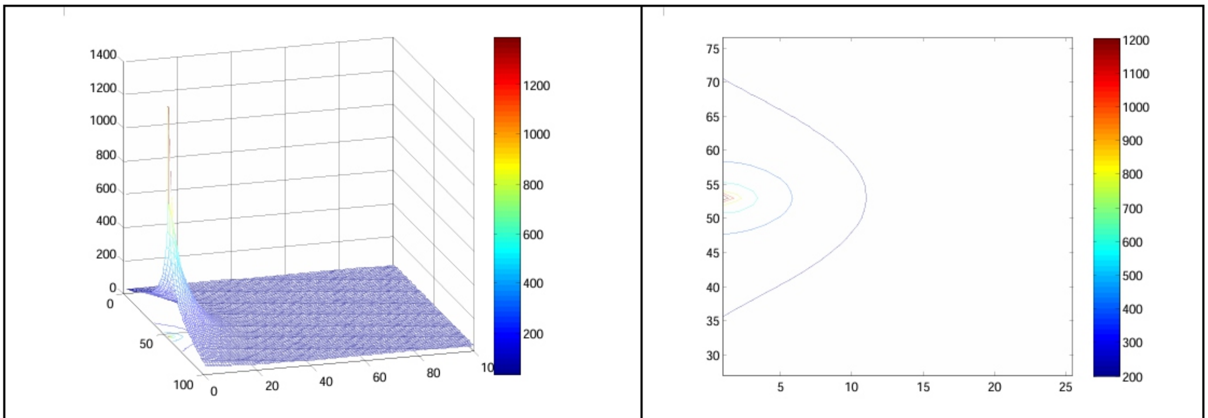

(a) Temperature distribution on surface of the substrate at 15. 5 sec	(b) Isotherm on substrate surface at 15. 5 sec

Figure 6: The temperature field of the substrate at 15. 5 sec for p = 5 Mpa, N = 100 RPM

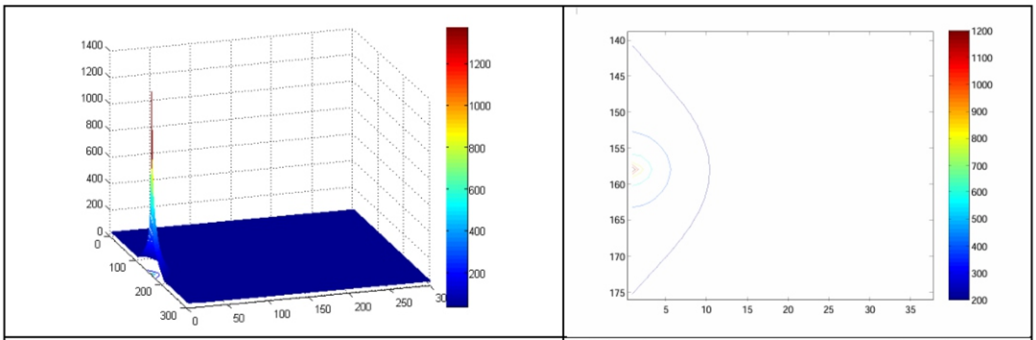

(a) Temperature distribution on the surface of the substrate at 30. 5 sec	(b) Isotherm on substrate at 30. 5 sec

Figure 7: The temperature field of the substrate at 30. 5 sec for p = 5 Mpa, N = 100 RPM

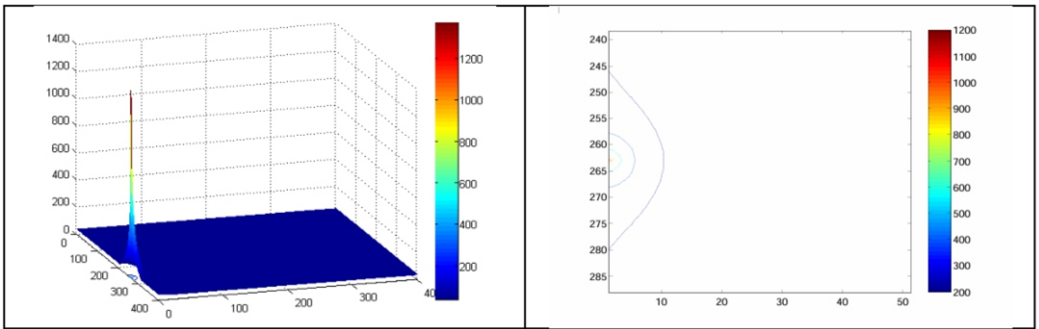

(a) Temperature distribution at 45. 5 sec	(b) Isotherm at 45. 5 sec

Figure 8: The temperature field of the substrate at 45. 5 sec for p = 5 Mpa N = 100 RPM

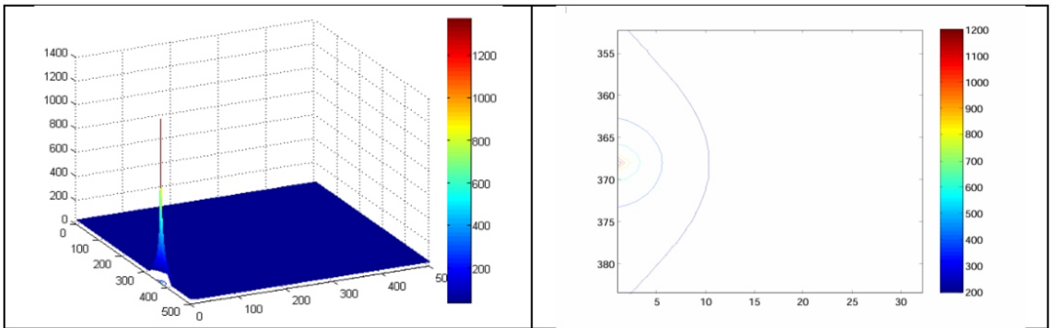

(a) Temperature distribution at 60. 5 sec	(b) Isotherm at 60. 5 sec

Figure 9: The temperature field of the substrate during steady surfacing at 60. 5 sec for p = 5 Mpa N = 100 RPM

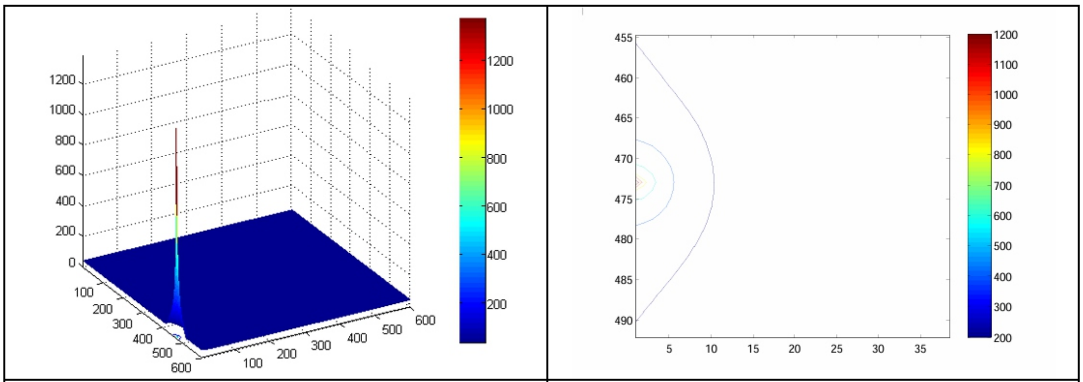

(a) Temperature distribution at 75. 5 sec	(b) Isotherm at 75. 5 sec

Figure 10: The temperature field of the substrate at 75. 5 sec for p = 5 Mpa N = 100 RPM

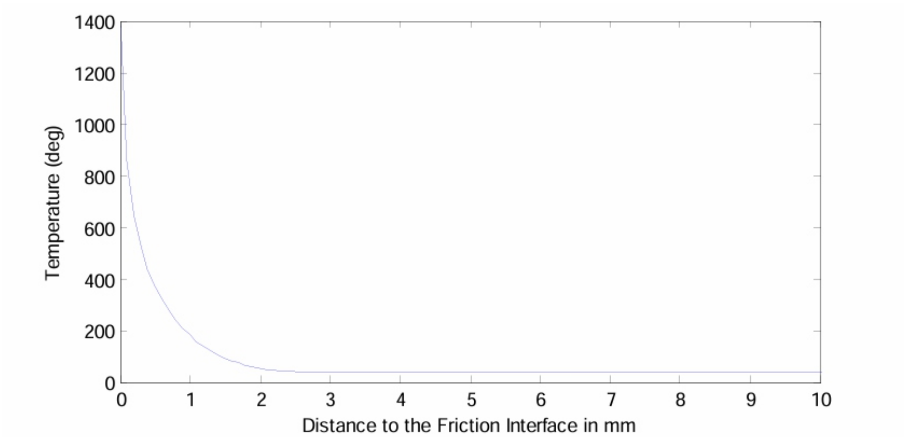

Figure 11: Simulation result of the temperature field of the substrate

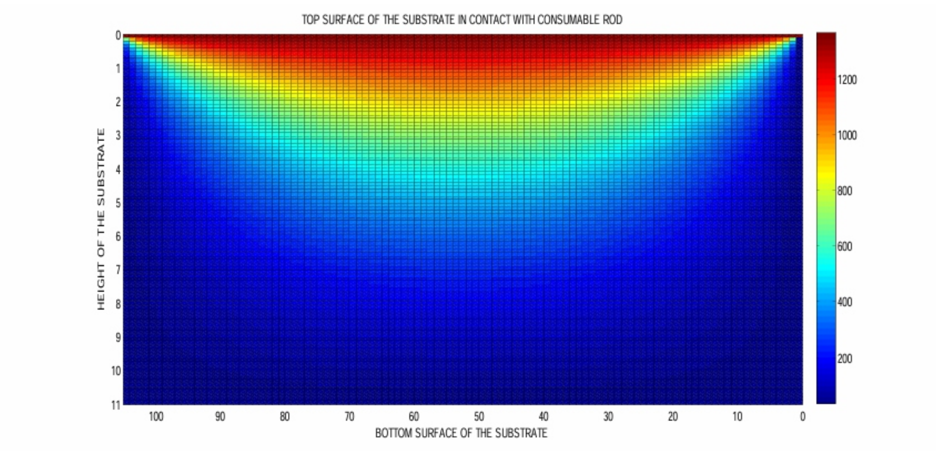

Figure 12: Temperature gradient along the depth of the substrate below consumable rod

4.CONCLUSIONS

1.The simulation program can assist in determining the feasible material combinations in Friction surfacing process.
2.The rubbing time required to reach forging temperature at 5MPa is 15 Sec and at 10 MPa is 9 Sec.
3.It is observed that effective forging takes place, if friction pressure of 5MPa and 300rpm, and friction pressure of 10 MPa and 100 rpm is used.
4.The thermal analysis showed that the HAZ is up to ≈ 3mm in low carbon steel substrate. The temperature range in HAZ is 1060oC to 1360oC.
5.The observation on setup of process parameters like preheating time for different matching factors, which allows for guidance in engineering applications.
6.The simulation results of consumable-rod and substrate can assist theoretical guidance in examining the feasibility and selection of primary process parameters in same field of research work in future.

ACKNOWLEDGEMENTS

The authors would like to thank Defence Metallurgical Research Laboratory (DMRL) Hyderabad, India, for their continued encouragement and permission to do experimental work. We also thank Princeton College of Engineering and Technology, Hyderabad, and JNTUH, Hyderabad for support and encouragement to do this research work.

REFERENCES

[1]. W. M. Thomas in "Proceedings of the first International Conference On Surface Engineering "(The Welding Institute, Abington, Cambridge, UK, 1987) p 261.
[2]. Grainger S, Blunt J. Engineering Coatings- design and application. 2nd ed. Cambridge; Abington; 1998.
[3]. Rafi, H. K., Balasubrahmanyam, K., Phanikumar, G., Rao, K. P., 2011. Thermal profiling using infrared thermography in friction surfacing, Metallurgical and materials Transactions A 42, 3425-3429.
[4]. Bedford G. M., Vitanov, V. I., Voutchlov, I. I., 2001. On the thermo- mechanical events during friction surfacing of high speed steels. Surface and Coating Technology 141, 34-39. doi:10. 10161/S0257-8772 (01)01129-X.
[5]. Fukakusa. K., 1996. On the characteristics of the rotational contact plane – a fundamental study of friction surfacing. Welding International 10, 524-529. doi: 10. 1080/09507119609549043.

[6]. V. I. Vitanov, I. I. Voutchkov (2005), "Process parameters selection for friction surfacing applications during Intelligent decision support, " J. Mater. Process. Technol. Vol. 159. pp, pp27-32.

[7]. V. I. Vitanov, I. I. Voutchkov, G. M. Bedford (2001), " Neurofuzzy approach to process parameter selection for friction surfacing applications, " Surf. Coat. Technol vol 140, pp 256-262.

[8]. V. I. Vitanov, I. I. Voutchkov, G. M. Fordford (2000), "Decision support system to optimise the Frictec (friction surfacing) process. " J. Mater. Process. Technol. Vol 107. Pp 236-242.

[9]. Verevikin, V. I., Druchinin, S. A., Koshelev, A. A., 2003. Calculation of parameters of friction surfacing regimes on basis of mathematical modeling, Izvestiya Utchebnykh Zavedenji, Chernaya Metallirgiya, 50-53.

[10]. Batchelor, A. W., Jana, S., Koh, C. P., Tan, C. S., 1996. The effect of metal type and multi-layering on friction surfacing. J. Mater. Proc. Technol. 57, 172-181.

[11]. M. Chandrasekaran, A. W. Batchlor, S. J. Jana (1998), "Study of the interfacial phenomena during friction surfacing of mild steel with tool steel and inconel. J. Mater. Sci Vol 33 pp 2709-2717.

[12]. M. Chandrasekaran, A. W. Batchelor, S. J. Jana (1997), " Study of the interfacial phenomena during friction surfacing of aluminum with steels, " J. Mater Sci Vol 32, pp 6055-6062.

[13]. H. Tokisue, K. Katoh, T. Usiyama, Mater Trans 47 (2006) 874.

[14]. Suhuddin SMU, Krohn H, Beyer M, Santos JF. Microstructural Evolution During Friction surfacing of Dissimilar Aluminum alloys, Metal Mater Trans A 2012; 43:5224.

[15]. Bedford, G. M. Vitanov, V. I.., Voutchkov, I. I., 2001. On the thermomechanical events during friction surfacing of highspeed steels. Surf. Coat. Technol. 141, 34-39.

[16]. Xuemei Liu, Junshan Yao, Xinhong Wang, Zengada Zou, Shiyao Qu "Finite difference modeling on the temperature field of consumable–rod in friction surfacing", Elsevier, Journal of materials processing technology 209(2009) 1392-1399.

[17]. X. M. Liu, Z. D. Zou, S. Y. Qu, J. S. Yao, " Finite Difference Modeling on the Temperature Field of substrate in Friction Surfacing" 2010 Second International conference on Computer Modeling and simulation, DOI 10. 1109/ICCMS 2010. 263., pp 360-364.

ISSN 09731784

Effectiveness and Overall Heat Transfer Coefficient of Fe3O4/Water Nanofluid Flow in a Double Pipe Heat Exchanger with Return Bend

N.T. Ravi Kumar1,* , L. Syam Sundar2 and P. Bhramara1
1 Department of Mechanical Engineering, J N T University-Hyderabad, India.
2A.M.R. Institute of Technology, Adilabad, Telangana (State), India.

ABSTRACT

The effectiveness and overall heat transfer coefficient of different particle concentrations of Fe3O4/water nanofluids flow in a double-pipe heat exchanger with return bend has been estimated experimentally under turbulent flow conditions. The experiments were conducted in the particle volume concentrations from 0.005% to 0.06% and in the Reynolds number range from 14000 to 30000. The enhancement of Nusselt number is about 15.6% at 0.06% volume concentration when compared to base fluid (water). The overall heat transfer coefficient for annulus-side is enhanced by 3.44%, tube-side is enhanced by 3.26% and the effectiveness of heat exchanger is enhanced by 1.008-times at 0.06% volume concentration at a Reynolds number of 28984 compared to water.

Keywords: *Double-pipe heat exchanger, Overall heat transfer coefficient, NTU, Effectiveness.*

1. INTRODUCTION

The double pipe heat exchangers are commonly used heat exchangers in commercial and industrial applications because of its small size, non-manufacturing difficulty and compactness. The base fluids generally used are water, ethylene glycol, propylene glycol, engine oil and etc. The performance of these base fluids can be enhanced by adding nano-sized particles. Choi [1] and his team developed high thermal conductivity fluids called as nanofluids, which is prepared by dispersing nanometer sized solid metallic particles in the fluids.

The use of nanofluids in double pipe heat exchangers and its convective heat transfer coefficient have been estimated by researchers and few of them are given below. Sarafraz and Hormozi [2] found heat transfer enhancement of 67% at 1.0% vol. of Ag/50:50% ethylene glycol/water nanofluid flow in a double pipe heat exchanger. ElMaghlany et al. [3] observed augmentation of effectiveness and the number of transfer units (NTU) of the double pipe heat exchanger using Cu/water nanofluids. Darzi et al. [4] estimated heat transfer and pressure drop of Al2O3/water nanofluid in a double pipe heat exchanger at different temperature range of working fluid. Hemmat Esfe and Saedodin [5] estimated convective heat transfer coefficient of MgO/water nanofluid flow in a double pipe heat exchanger at different particle concentrations 0.005, 0.01, 0.015, 0.02 and the nanoparticles diameter of 60, 50, 40 and 20 nm. Aghayari et al. [6] observed heat transfer coefficient and Nusselt number of 19% and 24% for 0.3% volume fraction of Al2O3/water nanofluid flow in a double pipe heat exchanger in counter flow direction. Abbasian Arani et al. [7] investigated heat transfer of TiO2/water nanofluids flow in a double pipe counter flow heat exchanger in the volume fraction range from 0.002 and 0.02 and the Reynolds number between 8000 and 51000. Sudarmadji et al. [8] prepared hot Al2O3/water nanofluid is flowing inside tube, while the cold water flows annulus tube and estimated heat transfer coefficient for 0.15%, 0.25% and 0.5% and observed Nusselt number increment of 40.5% compared to pure water under 0.5% volume concentration. Duangthongsuk and Wongwises [9] observed heat transfer enhancement of 6-11% at 0.2% volume concentration of TiO2/water nanofluid flow in a horizontal double tube counter flow heat exchanger under turbulent flow conditions. Sajadi and Kazemi [10] observed heat transfer enhancement of 22% at 0.25% of TiO2-water nanofluid flow in a double pipe heat exchanger in the Reynolds number of 5000. Huminic and Huminic [11] numerically investigated heat transfer characteristics of CuO and TiO2 nanofluids flow in a double-tube helical heat exchanger under laminar flow conditions and they observed significant enhancement of heat transfer with increase of particle concentration. Shakiba and Vahed [12] studied the hydro-thermal characteristics of Fe3O4/water nanofluid at 4.0% volume concentration in a counter flow double pipe heat exchanger using single phase model and control volume technique. Bahiraei and Hangi [13] studied the performance of Mn-Zn/water magnetic nanofluid flow in a counter flow double pipe heat exchanger under quadrupole magnetic field using the two-phase Euler–Lagrange method. Demir et al. [14] numerically studied the velocity and temperature profiles of water based TiO2 and Al2O3 nanofluids flow in a double pipe heat exchangers.

The further heat transfer enhancement in double pipe heat exchangers is possible by using return bend. Hong and Hrnjak [15] observed further heat transfer enhancement in pipes with return bend and they concluded with the effect of fluid mixing, hydrodynamic and thermal development of secondary flows at immediate downstream of the U-bend. Clarke and Finn [16] numerically investigated the heat transfer mechanism of secondary refrigerant flow in an air chiller U-bends and observed with return bend there is a 20% heat transfer enhancement for up to 20 pipe diameters. Other experimental investigations found that heat transfer may be enhanced immediately downstream of a U-bend [17,18]. Choi and Zhang [19] numerically investigated heat transfer of Al2O3/water nanofluid flow in a pipe with return bend and observed Nusselt number increase with increase of Reynolds number and Prandtl number, and the increment of specific heat of nanofluid. Prasad et al. [20] observed 25% heat transfer enhancement at 0.03% volume concentration of Al2O3/water flow in a double pipe heat exchanger with return bend and in the Reynolds number of 22000. The above works reveals there is a further heat transfer augmentation by modifying the geometry of the inner tube of double pipe heat exchanger. There is literature related to heat transfer, friction factor and effectiveness of magnetic nanofluids flow in a tube with return bends.

The overall heat transfer coefficient (tube-side and annulus-side) and effectiveness data for Fe3O4 nanofluid is not available in the literature. In this regard, the present investigation is carried for the estimation of overall heat transfer coefficient (tube-side and annulus-side) and effectiveness of Fe3O4 nanofluid experimentally. The experimental setup is fabricated and the experiments are conducted in the Reynolds number range from 14000 to 30000 and in the particle concentrations range from 0.005% to 0.06%.

2. EXPERIMENTAL SECTION

2.1. Preparation of nanofluids

The nanofluids of 0.005%, 0.01%, 0.03% and 0.06% volume concentrations were prepared by dispersing Fe3O4 nanoparticles (Sigma-Aldrich Chemicals, USA) in distilled water. The bulk quantity of 15 liters nanofluids were prepared and used in the experimental apparatus for the estimation of overall heat transfer coefficient and effectiveness. The surfactant of cetyl trimethylammonium bromide (CTAB) (1/10th of weight of nanoparticles) was used for uniform dispersion of nanoparticles in distilled water. The CTAB was initially mixed with 15 liters of distilled water and then stirred with high speed mechanical stirrer; after complete dispersion of surfactant the required quantity of Fe3O4 nanoparticles were added and continued stirring for 24 hours. The particles required for known percentage of volume concentration was calculated from the Eq. (1).

$$\phi = \frac{1}{(100/\varphi_m)(\rho_p/\rho_w)+1} \times 100\ (\%) \tag{1}$$

where $(\rho_p)$and (ρ_w) are the densities of the particles and water, respectively, and (ϕ) and (ϕ_m) are the volume and mass concentrations (%) of the dispersed fluid, respectively. The thermal properties of Fe_3O_4 nanofluids have been taken from the Sundar et al. [21] and the data is shown in **Table 1**.

Table 1: Thermophysical properties of base fluid and Fe3O4 nanofluid (Sundar et al. [21])

	T, (°C)	$\phi = 0.0\%$	$\phi = 0.005\%$	$\phi = 0.01\%$	$\phi = 0.03\%$	$\phi = 0.06\%$
(ρ),	20	998.5	998.8	999.10	999.7	1000.9
kg/m^3	40	992	992.3	992.60	993.21	994.42
	60	983.3	983.6	983.90	984.51	985.71
(k),	20	0.6024	0.604	0.6055	0.6087	0.6149
W/m K	40	0.6314	0.6341	0.6367	0.6421	0.6527
	60	0.653	0.6564	0.6598	0.6666	0.6802
(μ) ,	20	0.79	0.7916	0.7931	0.7963	0.8025
mPa.sec	40	0.54	0.5403	0.5406	0.5413	0.5425
	60	0.3	0.3009	0.3018	0.3038	0.3075
(C_p),	20	4182	4181.8	4181.5	4181.1	4180.2
J/kg K	40	4178	4177.8	4177.5	4177.1	4176.2
	60	4183	4182.8	4182.5	4182.1	4181.2
Prandtl	20	5.48	5.4766	5.4731	5.4663	5.4525
number (Pr)	40	3.57	3.5584	3.5468	3.5238	3.4775
	60	1.92	1.9163	1.9125	1.905	1.89

2.2 Experimental set-up and procedure

The experimental setup is shown in Fig. 1a and the test section details were shown in Fig. 1b. The experimental setup consists of two concentric tube heat exchangers, data logger along with personal computer, cooling water tank and heating water tank, a set of thermocouples, flow meters (both hot and cold). The test section is two double pipe heat exchangers and the inner tube is bent at a radius of 0.160 m at a length of 2.2 m. The effective length of the heat exchanger is 2.2 m, but the length of the inner tube is 5 m. The inner tube is made with stainless steel (SS304) material and the inner diameter is 0.019 m, outer diameter is 0.025 m. The annulus tube is made with Galvanised Iron (G.I.) and the inner diameter is 0.05 m, outer diameter (OD) is 0.056 m. In order to minimize the heat loss from the test section to atmosphere, the annulus tube is wound with asbestos rope insulation. The inlet and outlet temperatures of the hot fluid (water or nanofluid) and cold fluid were measured with four thermocouples. The thermocouples are connected with the data acquisition system and the readings are recorded in the computer for further calculations. The accuracy of thermocoused in this study is ±0.1 oC. The test section is designed in such a way that the hydrodynamically fully developed turbulent flow is maintained with the tube length/diameter ratio as 354. The mass flow rates of hot fluid (water or nanofluid) and cold fluid is controlled with the help of two rotameters. The arrangements of two double pipe heat exchangers are designed in such ways that, the flow path of the two fluids are in counter-flow direction. The hot Fe3O4 nanofluid (tube-side) inlet temperature of 60oC is maintained for the entire nanofluids inlet. The mass flow rate of nanofluids varies from 8 LPM to 14 LPM with an interval of 2 LPM. The temperature of the cold water (annulus-side) was maintained around 29oC and kept constant flow rate of 8 LPM (0.133 kg/s). The experiments were conducted at different particle concentrations of 0.005%, 0.01%, 0.03% and 0.06% and used one after another. The time taken to reach the steady state of the working fluids are 1 h and the final temperature values of cold and hot fluids were recorded for further overall heat transfer coefficient calculations. The logarithmic mean temperature difference method is used to calculate the inside and outside overall heat transfer coefficient of the nanofluids.

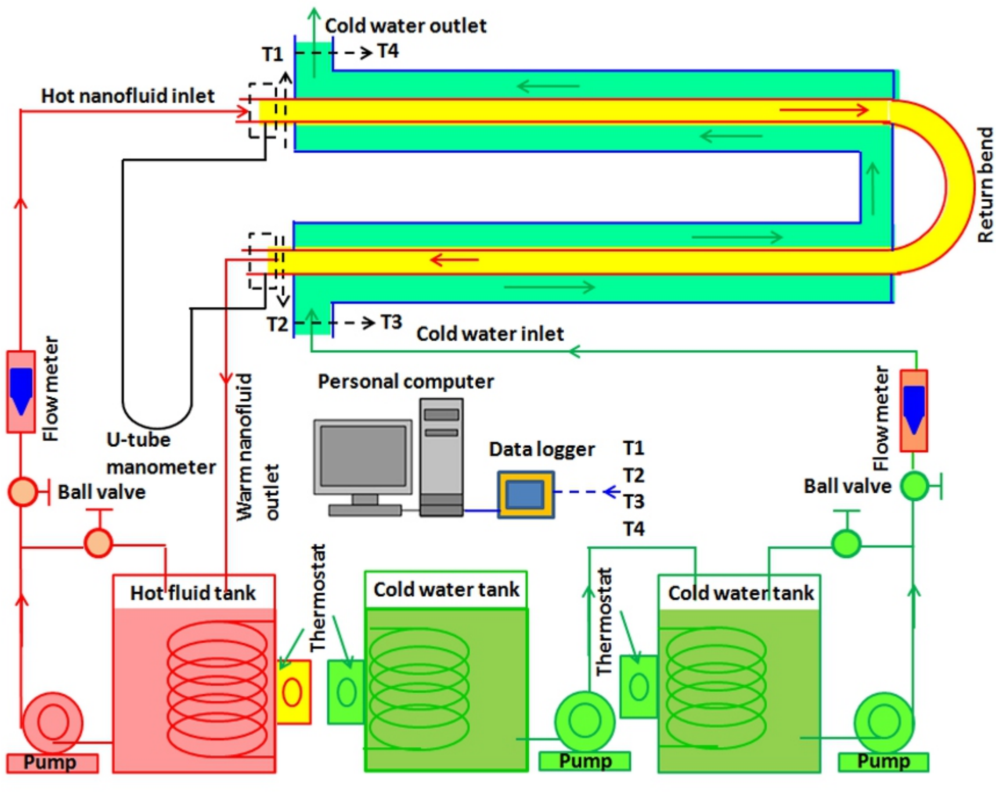

Fig. 1a Line diagram of an experimental setup

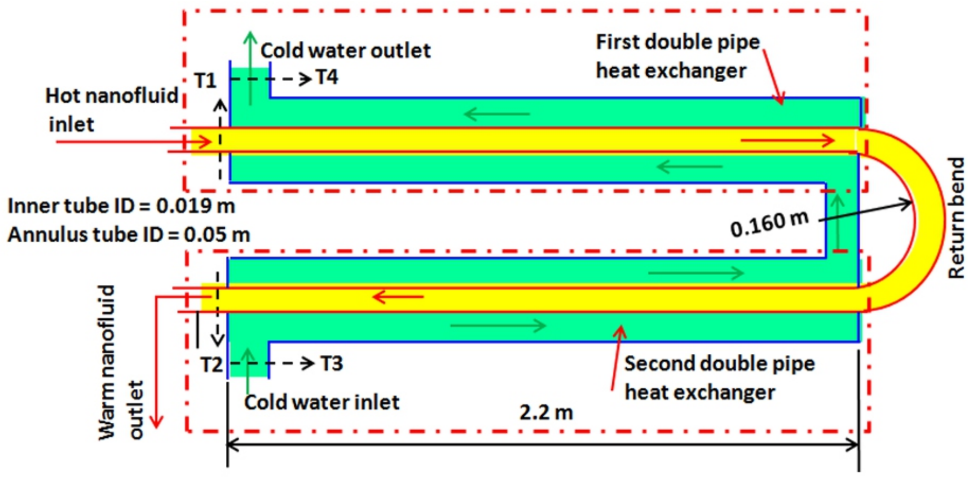

Fig. 1b Test section details

3. EXPERIMENTAL CALCULATIONS

3.1. Overall heat transfer coefficient

Rate of heat flow (tube side fluid), $Q_h = \dot{m}_h \times C_h \times (T_{h,i} - T_{h,o})$ (2)

Rate of heat flow (annulus side fluid), $Q_c = \dot{m}_c \times C_c \times (T_{c,o} - T_{c,i})$ (3)

Overall heat transfer coefficient (tube side), $U_i = \frac{Q_{avg}}{A_i\left(\frac{\Delta T_1 - \Delta T_2}{ln\left(\frac{\Delta T_1}{\Delta T_2}\right)}\right)}$ (4)

Overall heat transfer coefficient (annulus side), $U_o = \frac{Q_{avg}}{A_o\left(\frac{\Delta T_1 - \Delta T_2}{ln\left(\frac{\Delta T_1}{\Delta T_2}\right)}\right)}$ (5)

Where, $Q_{avg} = \frac{Q_h + Q_c}{2}$; $\Delta T_1 = T_{h,i} - T_{c,o}$; $\Delta T_2 = T_{h,o} - T_{c,i}$

For double pipe heat exchangers without considering the fouling factor term the below equation is used:

$$\frac{1}{U_i A_i} = \frac{1}{h_o A_o} + \frac{ln\left(\frac{D_o}{D_i}\right)}{2\pi KL} + \frac{1}{h_i A_i} \quad (6)$$

Where U_o or U_i is the overall heat transfer coefficients for annulus side and tube side, k is the thermal conductivity of tube material and L is the length of the heat exchanger.

The annulus heat transfer coefficient (h_o) is calculated based on the Gnielinski [22] and the expression is given below:

$$Nu_o = \frac{\left(\frac{f}{2}\right)(Re - 1000)\, Pr}{1.07 + 12.7\left(\frac{f}{2}\right)^{0.5}\left(Pr^{2/3} - 1\right)} \quad (7)$$

$$f = (1.58\, ln(Re) - 3.82)^{-2},\ 2300 < Re < 10^6,\ 0.5 < Pr < 2000$$

The obtained Nusselt number value from Eq. (7) is used to calculate the annulus heat transfer coefficient and the expression is given below:

$$h_o = \frac{Nu_o \times k_o}{D_h} \quad (8)$$

where D_h is the hydraulic diameter and k_o is the thermal conductivity of annulus fluid.

$$D_h = \frac{4A}{P} = D_o - D_i$$

where A is the flow area i.e. $A = \frac{\pi}{4}(D_o^2 - D_i^2)$

The h_o value from Eq. (8) is substituted in Eq. (6) for obtaining the tube side heat transfer coefficient (h_i or h_{nf}). That is the only unknown value in the equation. The value of Nu_{nf} can be determined as follows:

$$Nu_{nf} = \frac{h_{nf} \times D_i}{k_{nf}} \tag{9}$$

The Reynolds number is based on the flow rate at the inlet of the tube.

$$Re_{nf} = \left(\frac{\rho\, v\, d_i}{\mu}\right)_{nf} \tag{10}$$

The Prandtl number is calculated based on the specific heat, thermal conductivity, and viscosity of nanofluids at mean temperature of the fluid.

$$Pr_{nf} = \left(\frac{\mu C_P}{k}\right)_{nf} \tag{11}$$

3.2. Effectiveness – NTU method

Number of transfer units, $NTU = \frac{U \times A}{C_{min}} \Longrightarrow NTU = \frac{Q}{(\Delta T)_{LMTD} \times C_{min}}$ (12)

Heat capacity of tube side fluid, $C_h = \dot{m}_h \times C_h$ (13)

Heat capacity of annulus side fluid, $C_c = \dot{m}_c \times C_c$ (14)

where C_{min} is the smaller of C_c and C_h

Effectiveness, $\varepsilon = \frac{1-exp[-NTU(1-Z)]}{1-Z\, exp[-NTU(1-Z)]}$ (15)

where, $Z = \frac{C_{min}}{C_{max}}$

4. SAMPLE CALCULATIONS

4.1. Specifications

Annulus tube ID	= 0.05 m
Annulus tube OD	= 0.056 m
Radius of annulus (r_o)	= 0.025 m
Length of annulus (L_o)	= 4.4 m
Inner tube ID	= 0.019 m
Inner tube OD	= 0.025 m
Radius of inner tube (r_i)	= 0.0095 m

Inner tube OD	= 0.025 m
Radius of inner tube (r_i)	= 0.0095 m
Length of inner tube (L_i)	= 5 m
Area of annulus tube (A_o)	$= \pi D_o L_0$
	$= 3.14 \times 0.05 \times 4.52 = 0.7096\ m^2$
Area of inner tube (A_i)	$= \pi D_i L_i$
	$= 3.14 \times 0.019 \times 5 = 0.2983\ m^2$

4.2. Overall heat transfer coefficient

4.2.1. Annulus-side

Mass flow rate of annulus-side fluid,

$\dot{m}_c = 8\ \text{LPM} \Longrightarrow 8/60 \Longrightarrow 0.133\ \text{kg/sec}$

$m = \rho AV;\ V = \frac{m}{\rho A}$

Where A is the flow area, $A = \frac{\pi}{4}(0.05)^2 - \frac{\pi}{4}(0.025)^2 = 0.001471\ m^2$

$V = \frac{m}{\rho A} = V = \frac{0.133}{998.5 \times 0.001471} = 0.090\ m/sec$

$Re = \frac{\rho \times V \times D_h}{\mu}$

Where $D_h = 0.05 - 0.025 = 0.025\ m$

The Gnielinski [22] equation for turbulent flow inside the double pipe heat exchanger can be used to find the h_o value.

$$\frac{h_o D_h}{k_o} = Nu_o = \frac{\left(\frac{f}{2}\right)(Re - 1000)Pr}{1.07 + 12.7\left(\frac{f}{2}\right)^{0.5}(Pr^{2/3} - 1)}$$

$$f = (1.58 - \ln(Re) - 3.82)^{-2}$$

Where D_h is the hydraulic diameter.

$$D_h = \frac{4A}{P} = D_o - D_i$$

Where A is the flow area, $A = \frac{\pi}{4}(D_o^2 - D_i^2)$

$$Re_o = \frac{998.5 \times 0.090 \times 0.025}{0.000665} = 3378.38$$

$$Nu_o = \frac{\left(\frac{f}{2}\right)(Re - 1000)Pr}{1.07 + 12.7\left(\frac{f}{2}\right)^{0.5}(Pr^{2/3} - 1)}$$

Where, $f = (1.58 \ln(Re) - 3.82)^{-2}$

$f = (1.58 \ln(3378.38) - 3.82)^{-2} = 0.01234$

$$Nu_o = \frac{\left(\frac{0.01234}{2}\right)(3378.38-1000)Pr}{1.07+12.7\left(\frac{0.01234}{2}\right)^{0.5}(Pr^{2/3}-1)}$$

$$Nu_o = \frac{(0.00615)(2378.38)\times 4.525}{1.07+12.7\times 0.07842\times 1.735} = \frac{66.18}{2.7979} = 23.65$$

$$Nu_o = \frac{ho\times D_h}{k}$$

$$h_o = \frac{23.65\times 0.6169}{0.025} = 583.73\ W/m^2$$

4.2.2. Tube side

Mass flow rate of tube-side fluid, $\dot{m}_h = 8$ LPM $\Longrightarrow 8/60 \Longrightarrow 0.133\ kg/sec$

$m = \rho AV;\ V = \frac{m}{\rho\, A}$

where A is the flow area, $A = \frac{\pi}{4}(0.019)^2 = 0.0028\ m^2$

$$V = \frac{m}{\rho\, A} = V = \frac{0.133}{992\times 0.0028} = 0.4731\ m/sec$$

$$Re_i = \frac{\rho\times V\times d}{\mu}$$

$$Re_i = \frac{992\times 04731\times 0.019}{0.00054} = 16555.12$$

$$Pr_o = \frac{\mu\times C_p}{k} = \frac{0.00054\times 4178}{0.6314} = 3.57$$

$T_{h,i} = 50.2^oC,\ T_{h,o} = 43.5^oC,\ \ T_{c,i} = 28^oC,\ \ T_{c,o} = 34.3^oC$

Rate of heat flow (tube-side fluid), $Q_h = \dot{m}_h \times C_h \times (T_{h,i} - T_{h,o})$

$$= 0.133 \times 4178 \times (50.2 - 43.5) = 3732.3\ W$$

Rate of heat flow (annulus-side fluid), $Q_c = \dot{m}_c \times C_c \times (T_{c,o} - T_{c,i})$

$$= 0.133 \times 4178 \times (34.3 - 28) = 3509\ W$$

$$Q_{avg} = \frac{Q_h+Q_c}{2} \Longrightarrow \frac{3732.3+3509}{2} \Longrightarrow Q_{avg} = 3620\ W$$

Overall heat transfer coefficient (annulus-side), $U_o = \frac{Q_{avg}}{A_o(\Delta T)_{LMTD}}$

$$U_o = \frac{Q_{avg}}{A_o\left(\frac{\Delta T_1-\Delta T_2}{\ln\left(\frac{\Delta T_1}{\Delta T_2}\right)}\right)} \Longrightarrow \frac{3620}{0.609\times\left(\frac{(50.2-34.3)-(43.5-28)}{\ln\left(\frac{(50.2-34.3)}{(43.5-28)}\right)}\right)} = 325.01\ W/{}^oC$$

Overall heat transfer coefficient (tube-side), $U_i = \frac{Q_{avg}}{A_i(\Delta T)_{LMTD}}$

$$U_i = \frac{Q_{avg}}{A_i\left(\frac{\Delta T_1-\Delta T_2}{\ln\left(\frac{\Delta T_1}{\Delta T_2}\right)}\right)} \Longrightarrow \frac{3620}{0.2983\times\left(\frac{(50.2-34.3)-(43..5-28)}{\ln\left(\frac{(50.2-34.3)}{(43.5-28)}\right)}\right)} = 773.11\ W/oC$$

$$\frac{1}{U_i A_i} = \frac{1}{h_o A_o} + \frac{\ln\left(\frac{D_o}{D_i}\right)}{2\pi K L} + \frac{1}{h_i A_i}$$

$$\frac{1}{773.11\times 0.2983} = \frac{1}{584.45\times 0.7096} + \frac{\ln\left(\frac{0.05}{0.019}\right)}{2\times 3.14\times 45\times 4.4} + \frac{1}{h_i\times 0.2983}$$

$$(h_i)_{Exp} = 2875.73 \ \mathrm{W/m\,K}$$

$$\text{Nusselt number, } (Nu_i)_{Exp} = \frac{h_i\times D_i}{k} \Longrightarrow \frac{2875.73\times 0.019}{0.6314} = 86.54$$

4.2.3. Effectiveness ($\boldsymbol{\varepsilon}$) – NTU method

$$\text{Number of transfer units, } \ NTU = \frac{U\times A}{C_{min}}$$

Heat capacity of tube-side fluid,

$$C_h = \dot{m}_h \times C_h \Longrightarrow 0.133 \times 4178 = 555.67 \ \mathrm{J/sec\,K}$$

Heat capacity of annulus-side fluid,

$$C_c = \dot{m}_c \times C_c \Longrightarrow 0.133 \times 4182 = 556.2 \ \mathrm{J/sec\,K}$$

Where C_{min} is the smaller of C_c and C_h

$$NTU = \frac{773.11\times 0.2983}{555.67} = 0.415$$

$$\text{Effectiveness, } \varepsilon = \frac{1-\exp[-NTU(1-Z)]}{1-Z\exp[-NTU(1-Z)]}$$

$$\text{Where, } Z = \frac{C_{min}}{C_{max}}$$

$$Z = \frac{C_{min}}{C_{max}} \Longrightarrow \frac{415}{417.8} = 0.996$$

$$\text{Effectiveness, } \varepsilon = \frac{1-\exp[-NTU(1-Z)]}{1-Z\exp[-NTU(1-Z)]}$$

$$\varepsilon = \frac{1-\exp[-0.415\,(1-0.996)]}{1-0.996\times\exp[-0.415\,(1-0.996)]} = 0.293$$

5. RESULTS AND DISCUSSION

5.1. Overall heat transfer coefficient

In order to validate experimental apparatus, the initial heat transfer experiments were conducted with hot water, which is flowing inside the tube and cold water flowing inside annulus. The Eq. (9) is used to estimate the tube side Nusselt number and the data are shown in Fig. 2 along with water data. The difference between theoretical and experimental Nusselt number is ± 2.5%. So, it indicates that minimum heat loss takes place from an experimental apparatus to atmosphere. The nanofluids of different volume concentrations were introduced one by one into the experimental apparatus and the Nusselt number is calculated from Eq. (9) and the data is shown in Fig. 3. At same mass flow rate the

Nusselt number of nanofluid is more compared to water, which is possible with the dispersion of nanoparticles. At particle concentration of 0.005%, the Nusselt number enhancement is about 1.72% and 2.29% at Reynolds number of 16545 and 28954, respectively compared to water data. Similarly, at particle concentration of 0.06%, the Nusselt number enhancement is about 9.76% and 14.7% at Reynolds number of 16545 and 28954, respectively compared to water data. Within the measured Reynolds number range from 16545 to 28954, the Nusselt number enhancement is about 47.7%, 51.1%, 49.4% and 55.31% at 0.005%, 0.01%, 0.03% and 0.06% volume concentrations. The enhancement in heat transfer coefficient for nanofluid is caused due to the effective fluid mixing by providing the return bend for the test tube. The similar behavior of active method of heat transfer augmentation for Al2O3 nanofluid in a tube with return bend have been observed by Choi and Zhang [23] based on the numerical study.

The overall heat transfer coefficient (tube-side) of different particle concentrations of nanofluids estimated from Eq. (4) is shown in Fig. 4. The overall heat transfer coefficient (tube-side) is about 3.26% at particle concentration of 0.06% and at Reynolds number of 28954. Similarly, the overall heat transfer coefficient (annulusside) of different particle concentrations of nanofluids estimated from Eq. (5) is shown in Fig. 5. The overall heat transfer coefficient (annulus-side) is about 3.44% at particle concentration of 0.06% and at Reynolds number of 28954.

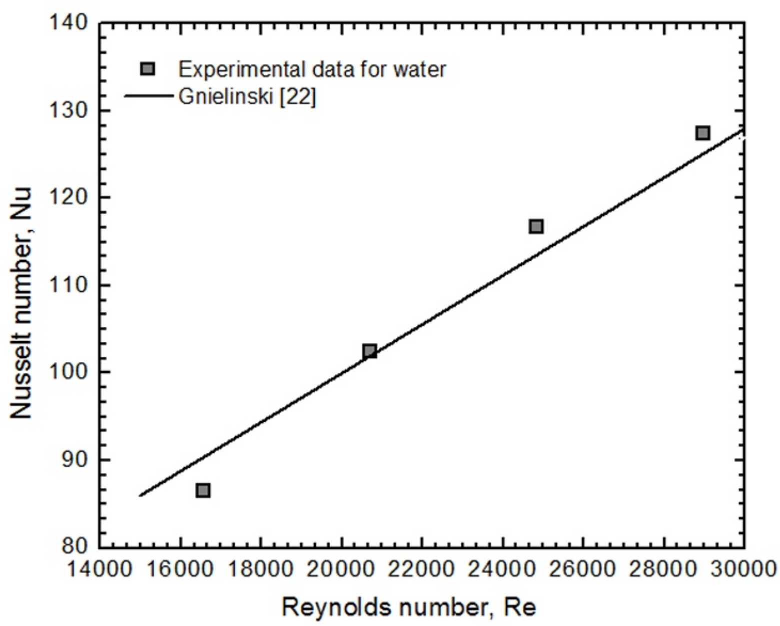

Fig. 2 The Nusselt number of hot water (tube-side) is compared with the literature values

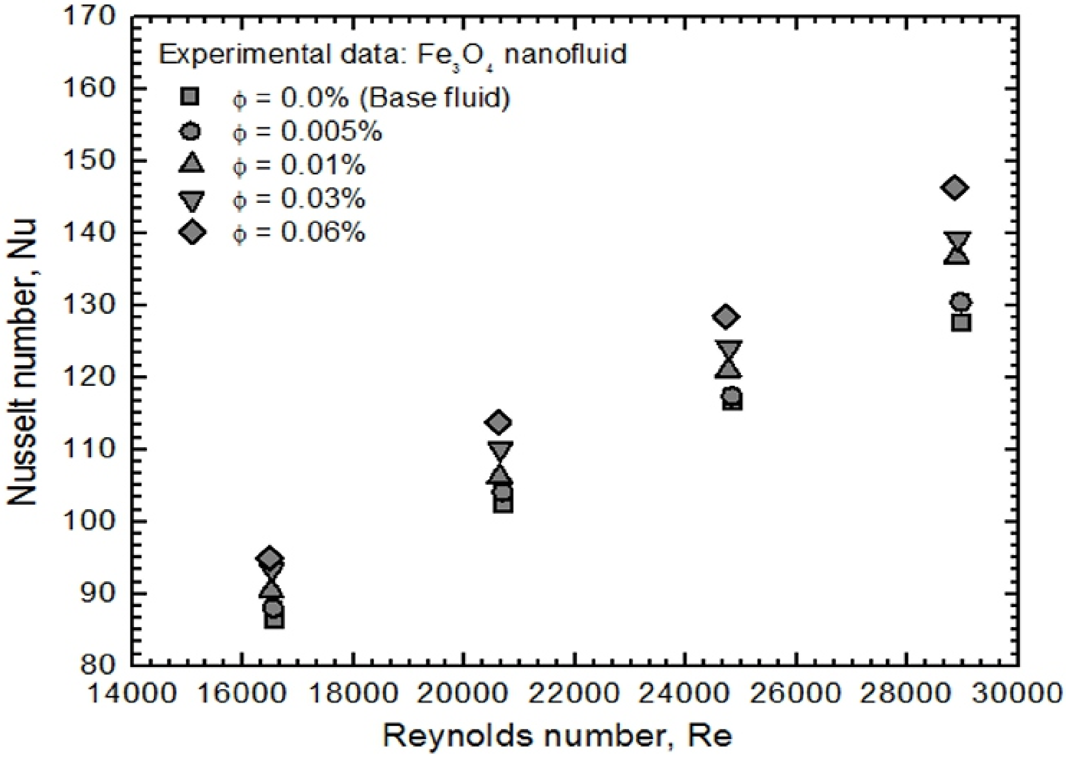

Fig. 3 The Nusselt number of hot Fe_3O_4 nanofluid (tube-side) at different particle concentrations and Reynolds number

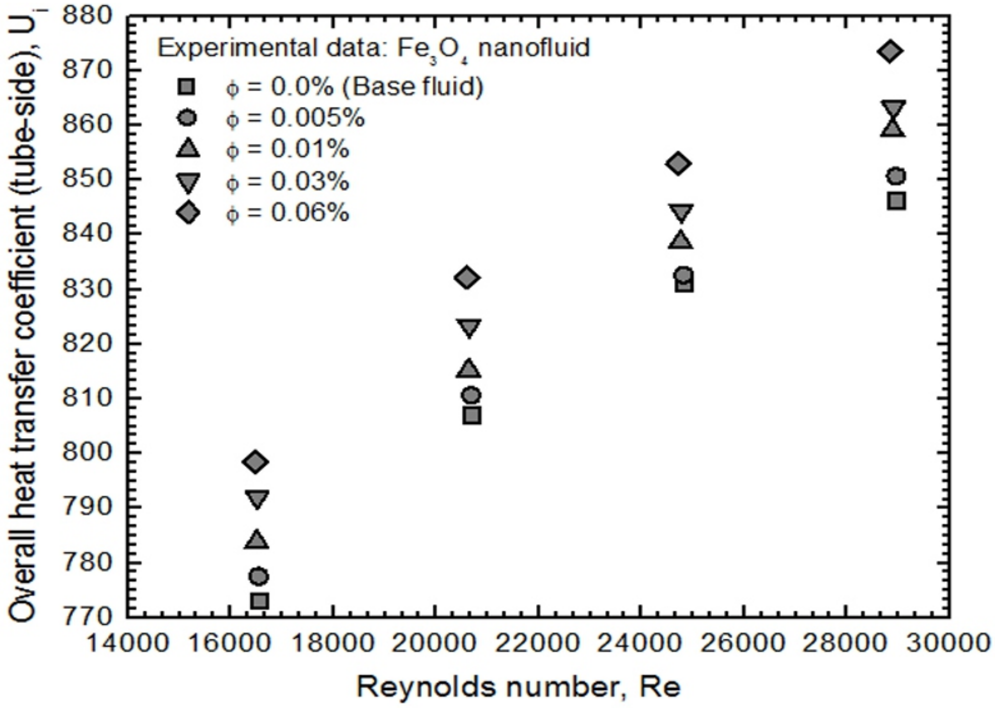

Fig. 4 Experimental overall heat transfer coefficient (tube-side) of hot Fe_3O_4 nanofluid at different particle concentrations and Reynolds number

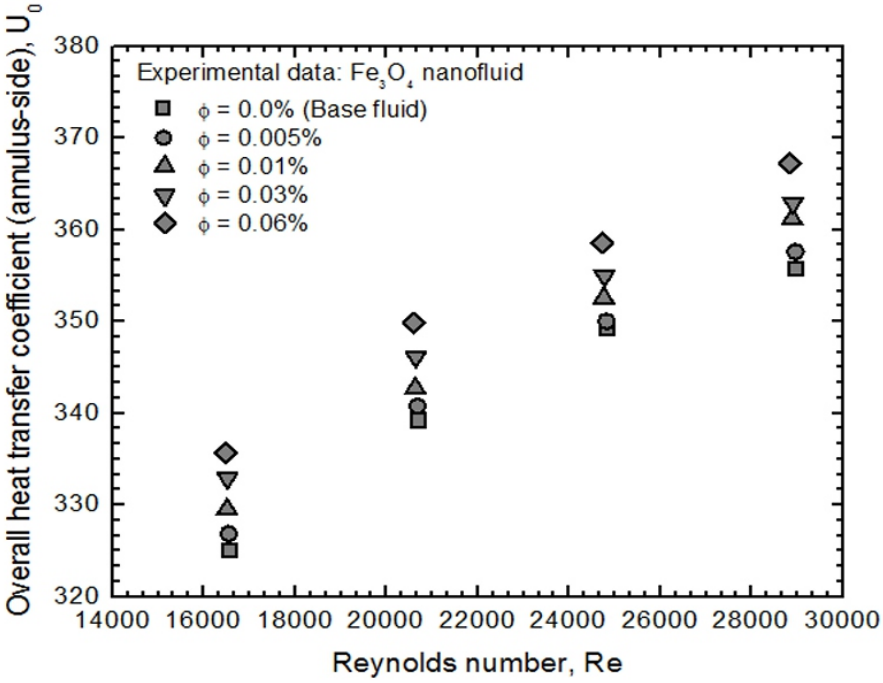

Fig. 5 Experimental overall heat transfer coefficient (annulus-side) of hot Fe_3O_4 nanofluid at different particle concentrations and Reynolds number

5.2. Effectiveness – NTU method

The performance of nanofluid flow in a double pipe heat exchanger is expressed in terms of effectiveness and number of transfer units (NTU). The higher value of effectiveness) and NTU indicates the higher performance of heat exchanger. The mass flow rates of both hot nanofluid and cold fluid were used for the calculation of effectiveness) and NTU. The Eq. (12) is used to calculate the NTU of water and nanofluids based on the overall heat transfer coefficient, flow area and minimum heat capacity between hot and cold fluids. The obtained values were shown in Fig. 6. It is observed from the figure, the NTU of water is 0.415 and 0.452 at Reynolds numbers of 16554 and 28970. Similarly, the NTU of 0.06% of nanofluid is 0.429 and 0.469 at same Reynolds numbers of 16554 and 28970. This indicais 0.429 and 0.469 at same Reynolds numbers of 16554 and 28970. This indicates that, with the use of nanoparticles in the base fluid (water), the NTU increases.

The Eq. (15) is used to estimate the effectiveness of water and nanofluids and the data is shown in Fig. 7. It is observed from the figure, the effectiveness of water is 0.293 and 0.339 at Reynolds numbers of 16554 and 28970. Similarly, the effectiveness of 0.06% of nanofluid is 0.3002 and 0.3418 at same Reynolds numbers of 16554 and 28970. At all the operating parameters, the addition of the nanoparticles in the base fluid (water) enhances the overall heat transfer coefficient and, accordingly, the effectiveness and NTU. Finally, addition of nanoparticles in the base fluids enhances the heat exchanger performance, but penalty in the pumping power is also there. Compared to heat transfer

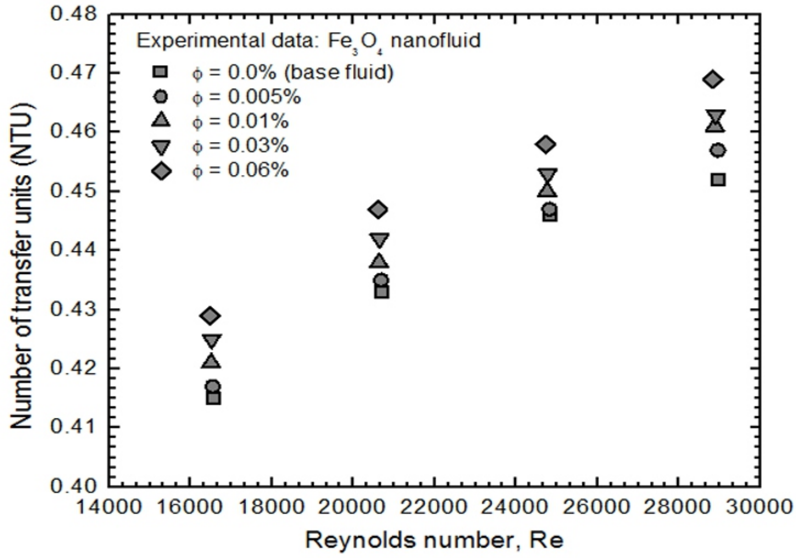

Fig. 6 Number of transfer units (NTU) variation for water and nanofluids at different Reynolds numbers

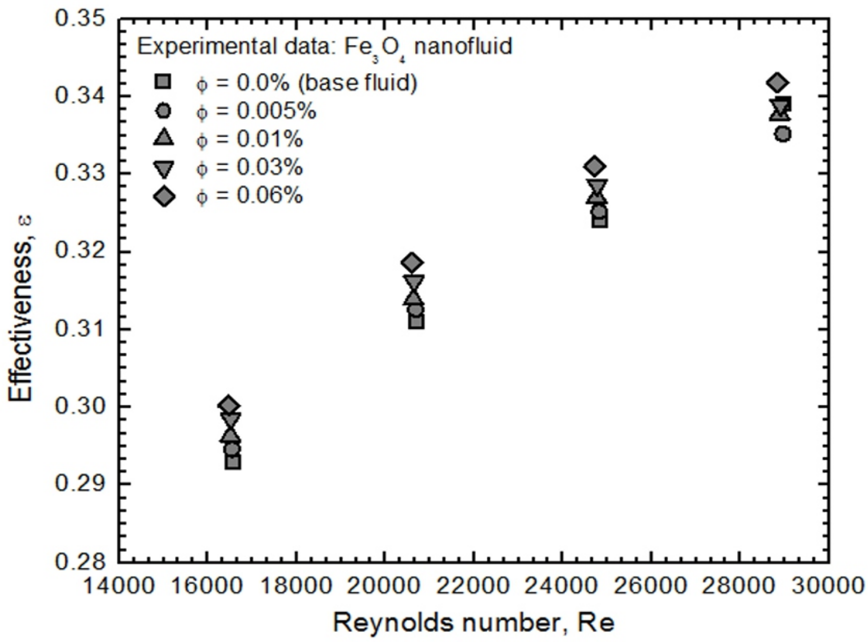

Fig. 7 Effectiveness (ε) variation for water and nanofluids at different Reynolds numbers

The enhancement of Nusselt number is about 15.6% at 0.06% volume concentration when compared to base fluid (water).

The overall heat transfer coefficient for annulus-side is enhanced by 3.44%, tube-side is enhanced by 3.26% and the effectiveness of heat exchanger is enhanced by 1.008-times at 0.06% volume concentration at a Reynolds number of 28984 compared to water.

The NTU is enhanced by 1.037-times and the effectiveness by 1.024-times for 0.06% nanofluid at Reynolds number of 28970.

The use of Fe3O4 nanoparticles in the base fluid cause higher Nusselt number, overall heat transfer coefficient and effectiveness because of micro-convection and Brownian motion of particles.

Nomenclature

C_p Specific heat, $J/kg\ K$

d Inner diameter of the tube, m

f Friction factor

h Heat transfer coefficient, $W/m^2\ K$

k Thermal conductivity, $W/m\ K$

L Length of the tube, m

$\dot{m}$ Mass flow rate, kg/sec

Nu Nusselt number, $h\ D/k$

Pr Prandtl number, $\mu\ C/k$

Q Heat flow, $Watts$

Re Reynolds number, $4\ \dot{m}/\pi\ D\mu$

v Velocity, m/sec

Greek symbols

Δ Uncertainty

Δp Pressure drop

ϕ Volume concentration of nanoparticles, 9

μ Dynamic viscosity, $kg/m^2\ sec$

ρ Density,kg/m^3

Subscripts

b Bulk temperature

c Cold

Exp Experimental

h Hot

i Inlet

o Outlet

p Particle

Reg Regression

w Water

REFERENCES

S.U.S. Choi, Enhancing thermal conductivity of fluids with nanoparticles. In Proceedings of the 1995 ASME International Mechanical Engineering Congress and Exposition San Francisco, CA, USA, 1995.

M.M. Sarafraz, F. Hormozi, Intensification of forced convection heat transfer using biological nanofluid in a double-pipe heat exchanger, Experimental Thermal and Fluid Science 66 (2015) 279–289.

W.M. El-Maghlany, A.A. Hanafy, A.A. Hassan, M.A. El-Magid, xperimental study of Cu–water nanofluid heat transfer and pressure drop in a horizontal double-tube heat exchanger, Experimental Thermal and Fluid Science 78 (2016) 100–111.

A.A.R. Darzi, M. Farhadi, K. Sedighi, Heat transfer and flow characteristics of Al2O3–water nanofluid in a double tube heat exchanger, International Communications in Heat and Mass Transfer 47 (2013) 105–112.

M. Hemmat Esfe, S. Saedodin, Turbulent forced convection heat transfer and thermophysical properties of MgO–water nanofluid with consideration of different nanoparticles diameter, an empirical study, J Therm Anal Calorim 119 (2015) 1205–1213.

R. Aghayari, H. Maddah, M. Zarei, M. Dehghani, S.G.K. Mahalle, Heat transfer of nanofluid in a double pipe heat exchanger, International Scholarly Research Notices Article ID 736424 (2014) 1–7.

A.A.A. Arani, J. Amani, Experimental study on the effect of TiO2–water nanofluid on heat transfer and pressure drop. Exp Thermal Fluid Science 42 (2012) 107–115.

S. Sudarmadji, S. Soeparman, S. Wahyudi, N. Hamidy, Effects of cooling process of Al2O3-water nanofluid on convective heat transfer, Faculty of Mechanical Engineering Transactions 42 (2014) 155–161.

W. Duangthongsuk, S. Wongwises, Heat transfer enhancement and pressure drop characteristics of TiO2–water nanofluid in a double-tube counter flow heat exchanger, International Journal of Heat and Mass Transfer 52 (2009) 2059–2067.

A.R. Sajadi, M.H. Kazemi, Investigation of turbulent convective heat transfer and pressure drop of TiO2/water nanofluid in circular tube, Int. Communications in Heat and Mass Transfer 38 (2011) 1474–1478.

G. Huminic, A. Huminic Heat transfer characteristics in double tube helical heat exchangers using nanofluids, International Journal of Heat and Mass Transfer 54 (2011) 4280–4287.

A. Shakiba, K. Vahedi, Numerical analysis of magnetic field effects on hydro-thermal behavior of a *magnetic nanofluid in a double pipe heat exchanger, Journal of Magnetism and Magnetic Materials, 402 (2016) 131142.*

M. Bahiraei, M. Hangi, Investigating the efficacy of magnetic nanofluid as a coolant in double-pipe heat exchanger in the presence of magnetic field, Energy Conversion and Management, 76 (2013) 1125–1133.

H. Demir, A.S. Dalkilic, N.A. Kürekci, W. Duangthongsuk, S. Wongwises, Numerical investigation on the single phase forced convection heat transfer characteristics of TiO2 nanofluids in a double-tube counter flow heat exchanger, International Communications in Heat and Mass Transfer 38 (2011) 218–228.

S.H. Hong, P. Hrnjak, Heat transfer in thermally developing flow of fluids with high Prandtl numbers preceding and following U-bend, ACRC Report CR-24, University of Illinois, Urbana, IL, 1999.

R. Clarke, D.P. Finn, The influence of secondary refrigerant air chiller Ubends on fluid temperature profile and downstream heat transfer for laminar flow conditions, International Journal of Heat and Mass Transfer 51 (2008) 724–735.

A.J. Ede, The effect of a 180o bend on heat transfer to water in a tube, in: Proceedings of the Third International Heat Transfer Conference, Chicago, 1966, pp. 99–104.

M. Moshfeghian, Fluid flow and heat transfer in U-bends, PhD Thesis, Oklahoma State University, Stillwater, 1978.

J. Choi, Y. Zhang, Numerical simulation of laminar forced convection heat transfer of Al2O3-water nanofluid in a pipe with return bend, International Journal of Thermal Sciences 55 (2012) 90–102.

P.V. Durga Prasad, A.V.S.S.K.S. Gupta, M. Sreeramulu, L. Syam Sundar, M.K. Singh, A.C.M. Sousa, Experimental study of heat transfer and friction factor of Al2O3nanofluid in U-tube heat exchanger with helical tape inserts, Experimental Thermal and Fluid Science, 62 (2015) 141–150.

L.S. Sundar, M.K. Singh, A.C.M. Sousa, Investigation of thermal conductivity and viscosity of Fe3O4 nanofluid for heat transfer applications, International Communications in Heat and Mass Transfer 44 (2013) 7–14.

V. Gnielinski, New equations for heat and mass transfer in turbulent pipe and channel flow, Int. Chem. Eng. 16 (1976) 359–368.

J. Choi, Y. Zhang, Numerical simulation of laminar forced convection heat transfer of Al2O3/water nanofluid in a pipe with return bend, Int. J. Therm. Sci. 55 (2012) 90–102.

ISSN 09731784

Design and Analysis of an Axial Fan used in Kiln Shell Cooling

Parasaram Sarath Chandra1, Dr. K. Sivaji Babu2 and U. Koteswara Rao3
M.Tech (Machine Design) Research student1, PVPSIT, Kanuru, India. Principal2, Department of Mechanical Engineering, PVPSIT, Kanuru, India. Associate Professor3, Department of Mechanical Engineering, PVPSIT, Kanuru, India.

ABSTRACT

The design of high efficient fans is often based on the experience of the designer. Based on the integral parameters of the flow and the geometry of an axial flow fan; a performance analysis of it has been performed. The main scope of the design process of axial fans, employs either airfoil theory or more direct design methods is to deliver high efficiency blades. Three aerofoils have been studied for the application and finally a combination of airfoil literally called Fseries had been used in the present work. An existing axial fan has been considered for efficiency improvement where airfoil theory in combination with free vortex design method, is used for a design advantage.

The effectiveness of the design procedure is verified with CFD simulation. The experience acquired from the analysis of the performance of the preliminary design, came in handy in later stages of design in order to achieve the best efficiency possible, which is an iterative process. The target of improved static efficiency (higher than 67%) has been achieved and it's been calculated as 71%. Performance of the design fan has been investigated by means of ANSYS CFX, a commercial CFD software. In this paper, theoretical results obtained are compared by drawing a performance curve, with those results obtained CFD simulation.

Keywords: *Turbomachines, axial fans, aerofoils, free vortex theory, CFD*

I. INTRODUCTION

Modern cement plants needs a wide range of process fans. Process critical fans can be mainly classified as centrifugal and axial type of fans. Here, the author employs the design of axial fan used to cool a clinker rotary kiln shell. Overall capacity of the plant is generally determined by the capacity of clinker rotary kiln. So, the mechanics of rotary kiln cylinder is paid close attention on engineering sites due to its frequent damage and expensive maintenance cost.

The main focus of the paper was to design and analyse an axial fan with improvised efficiency, by using an industrial example for demonstration purpose and establish a systematical design procedure which predicts the fan performance where usage of computational fluid dynamics (CFD) will be instrumental. High volume flow and low pressure fans are used in cooling applications for several process equipment and also for ventilation of silo cones, mines etc. Present paper focuses on a specific application, related to clinker kiln-shell cooling.

Present work deals with axial flow fan of type power absorbing turbomachines. The flow in the investigated form, i.e., air, is characterised by Mach numbers below the compressibility limit (< 0.3). It is a clear case that fan operating with incompressible flow, which is a type of high capacity, low head (pressure), and single stage axial flow type turbomachine.

Fans are a kind of equipment where we can use engineering strategies and optimize the energy consumption without effecting their efficiency. An axial flow fan can achieve high efficiencies as with an optimum blade settings and is only slightly lower than that obtained with the backward inclined aerofoil centrifugal fan and much better than convectional fans [18].

To cool a kiln-shell used in cement plant needs a fan with specific speeds which works for given site conditions. Selection of a fan and design of an impeller needs a keen study of rotor blade design which is majorly based on velocity components. The blade may be of simply a plate with camber angles or an aerofoil shape [4]. Research is suggesting that replacing the curved camber plate with the aerofoil blade may produce almost identical performance but which results in the considerable increase in the total efficiency as well as in structural strength of the blade.

Designing an efficient airfoil profile implies that the shape which thus acquired has to be aerodynamically efficient. A comprehensive aerodynamic treatment of it, has been presented in the present work. Airfoil and the blade so designed are analysed using commercial CFD software called ANSYS CFX. The main emphasis will be on improvement of efficiency and the system performance.

The design of high efficient fan is often based on the experience of a designer. In order to determine the dimensions of a fan, one can use either Cordier diagram or background curves. Cordier diagram [9] provides an optimum dimensions for a fan as a system, whereas through background curves, system and blade geometries could be approximately estimated and refined for actual design point based on well-established design procedure. The present paper sees, the use of both in a blend for optimum values and to attain best efficiency point.

Fan characteristics can be described by consistent parameters such as volume flow rate, pressure, power, and efficiency.

An industrial example, upon industrial study, has been considered for the demonstration of the design flow. Based on specifications of site conditions and flow requirements, a preliminary calculations has been made which defined the system resistance. From these considerations a specific valve of fan diameter has obtained, by using Cordier diagram which was verified with background fan curves for an optimal value.

II. DESIGN APPROACH

A. Fan Theory

The rotor design is a function of swirl coefficient and flow coefficient. Swirl is an important measure of rotor torque. In this method, static and total pressure were normalized by using non-dimensional terms of axial velocity and dynamic pressure. Based upon initial calculation of pressures, velocity of air, speed of an impeller within the system resistance with trial and error method will give non-dimentionalized factors like load factor, specific speed and specific diameter. Load factor was determined to be 1.15, shown in figure 1

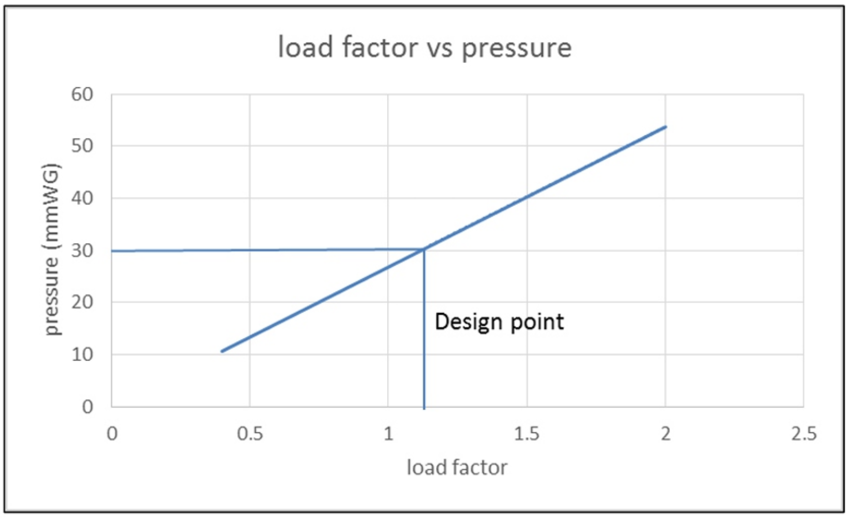

Fig. 1 load factor vs static pressure

If the fan and hub diameter are known, then the total pressure rise and the volumetric flow rate can be converted into non-dimensional quantities. It is possible to estimate the fan diameter and hub diameter using Cordier diagram [9] which needs a parameter called specific speed.

$$\text{Specific speed; } N_s = N \,.\, Q^{\frac{1}{2}} \,.\, \Delta P^{\frac{-3}{4}}$$

Where N is the fan rotational speed in rpm, Q is the volumetric flow rate in m^3/s and ΔP is the total pressure rise across the fan in Pascal.

The general momentum equation can be written in Z and Y direction and given as follows:

$$Z = \left[\rho.s.dr.{V_{a1}}^{2} - \int_0^s \rho\,.dr.{V_{a2}}^{2}.dy\right] + [p1.s.dr - \int_0^s p2.dr.dy]$$

$$Y = [\rho \,.\, s.\, dr.\, V_{a1}.\, V_{\theta 1}] - [\int_0^s \rho.\, drVa2.\, V\theta 2dy] + E$$

Z and Y are the forces acting on the blade element of length 'dr' for constant inlet velocity. 'E' in equation related to 'Y' is the shear stress term due to wake flow shown in Figure 2.

Assume, as the E is negligible with constant velocity, and at Y direction pressure at inlet and exit do not tend to change. The simplified relations are as follows;

$$Z = (p1\text{-}p2).\ s.\ dr$$

$$Y = \rho.s.\ V_a.\ (V_{\theta 1} - V_{\theta 2}).\ dr$$

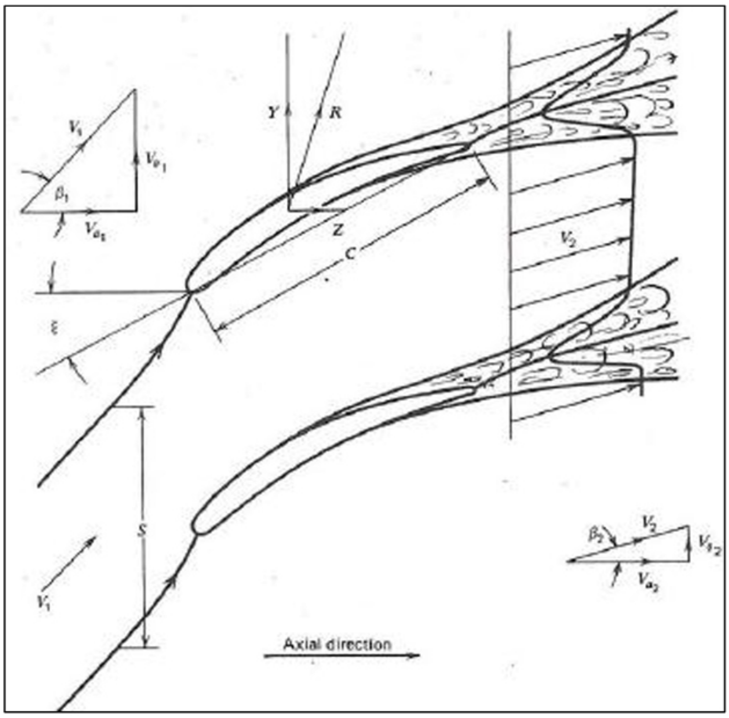

Fig. 2 Flow representation with cascade in a blade [3]

Thus exerted, theoretical pressure can be given as follow;

$$\Delta p_{th} = p_2 - p_1 + w$$

Where, 'w' is the mean total pressure loss due to the presence of wake, which is assumed as negligible in this case.

The efficiency of the fan unit is influenced by the amount of swirl left in the air after it has passed the last stage of blading in the unit. The swirl momentum can play no part in overcoming the resistance of the duct system unless the associated tangential component is removed and its velocity head converted into static pressure. Furthermore as per Wallis [3], wake consideration is not necessary factor in fan design but a considerable understanding should be needed for studying the effects of noise and blade vibration.

Theoretical head rise w.r.t present design considerations could be written as;

$$\frac{\Delta P}{0.5\ \rho.{V_a}^2} = k_h - k_R$$

Swirl coefficient which is a measure of rotor torque can be defined as the ratio of the swirl velocity and the axial velocity at a given radius.

$$\varepsilon = \frac{V_\theta}{V_a}$$

Flow coefficient can be defined as, the ratio of the axial velocity and rotational rotor speed at a given radius.

$$\lambda = \frac{V_a}{\Omega . r}$$

So, the theoretical pressure rise coefficient can be given as;

$$K_h = \left(\frac{2}{\lambda}\right) . \varepsilon$$

The relative velocity and absolute velocity factors play key role in estimating pressure ratios, blade angle while designing a blade. As per the free vortex theory, the axial velocity component is constant throughout the fan annulus. There is no radial velocity component and the pressure rise is constant in radial direction [6].

Axial velocity is calculated from the continuity equation.

$$V_a(u) = \frac{A_{fan} . V_{fan}}{A_{annulus}} = \frac{Q_{fan}}{\frac{\pi}{4} . (D_{fan}^2 - D_{hub}^2)}$$

The flow over the rotor blades can be represented by either absolute velocities or relative velocities. The schematics of velocity vectors for relative and absolute velocities are shown in figure 3.

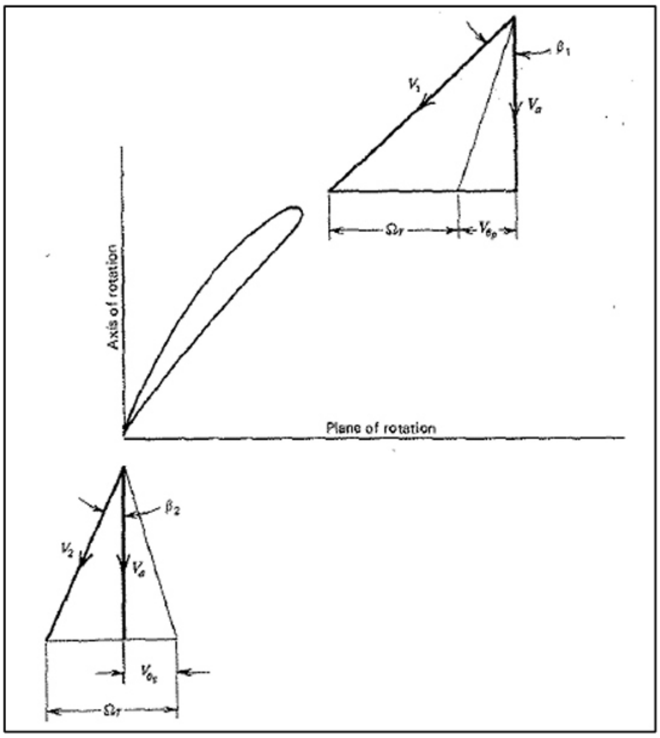

Fig. 3 Absolute velocity vector [6]

The relative flow angles with respect to the rotor blades are calculated by using equations;

$$\beta 1 = \text{atan}\left(\frac{1}{\lambda}\right)$$

$$\beta 2 = \text{atan}\left(\frac{1-\varepsilon}{\lambda}\right)$$

$$\tan(\beta m) = 0.5(\tan(\beta 1) + \tan(\beta 2))$$

The thrust and torque exerted on the flow by the rotor blades can be calculated by using the following equations. The torque acting on the rotor shaft can be expressed in terms of the swirl momentum added to the stream.

$$T = T_c * 0.5\,(\rho\,.\,u\,.\,\pi\,.\,r_{tip}^3)$$

$$T_c = 4\,.\frac{x^3}{3}\,.\,\varepsilon$$

The main interest in design with the thrust produced by the rotor is in relation to the design of thrust bearings and supports. This could be compensated with an estimate based on the pressure rise across the rotor and the swept area.

$$T_h = T_{hc} * 0.5 * (\rho\,.\,u^2\,.\,\pi.\,r_{tip}^2)$$

$$T_h = \frac{\Delta p.\,x.\,r}{0.5.\,(\rho.\,u^2)}$$

B. Procedure and calculations

The fan design is an iterative process. For starting the calculations with efficiency assumed to 89% as an initial guess. With blading design in process, efficiency is calculated and checked for convergence. Diffusion efficiency was considered as 80%. Static pressure recovery is assumed as 80%. Tip clearance was chosen to be 2.5% of blade span.

Table -1 Specifications

Specification of a fan	
Volumetric flow, m^3/s	5
Static pressure, Pa	300
Density, Kg/m^3	1.07
Speed, rpm	1450
Fan diameter, m	0.8

Hub to tip ratio has been chosen for feasible hub diameters from minimum hub diameter to the maximum possible one. Minimum hub diameter can be given as,

$$d_{min} = \frac{30.5932 \,.\, \sqrt{P_s}}{rpm}$$

Among five different feasible combinations of hub to tip ratios (x), one was chosen based on best efficiency, and estimates on component losses in the fan unit and a prediction of overall efficiency with an appropriate convergence. Estimates to loss in components had been followed by a graphical procedure prescribed by Wallis [6]. Later rotor design with moments based on non-dimensional coefficients with the dimensional quantities, as computed by the modified isolated airfoil theory which uses free vortex design method.

With these respects, hub to tip ratio was selected to be 0.5 which gave 71% total to static efficiency an increase of 4% with the existing one which is a significant one when implemented in industry.

The efficiency loss due to profile drag Cdp, were aimed at keeping either the blade element efficiency or the lift coefficient constant along the blade. The blade lift and drag coefficients are related by equation, blade loading;

$$C_l \,.\, \sigma = 2 \,.\, \varepsilon \,.\, \cos(\beta m)$$

Solidity; $\sigma = (c/s)$

From the two empirical equations above, C_l is obtained which is an approximation of total lift coefficient. The chord has been chosen with a view to keeping the blade aspect ratio approximately 2.

Primary drag coefficient is found to be 0.011 for the design of hub to tip ratio of 0.5. Secondary drag coefficient is an estimate based on the consideration of airfoil and cambered plate with constant thickness assumptions.

$$C_{ds} = 0.018 * \; C_l^2 - - - - -\rightarrow for\; airfoil$$

So the total drag coefficient is, $C_d = C_{dp} + C_{ds}$

As the free vortex design assumption, the total head rise coefficient and the axial velocity component, are both constant along the blade span.

Rotor loss coefficient is calculated by following equation;

$$\frac{K_R}{K_h} = \frac{\lambda}{\frac{C_l}{C_d}\cos(\beta m)}$$

Finally efficiency can be calculated by equation;

$$\eta = 1 - \frac{K_R}{K_h}$$

The detailed design of fan blade elements is followed by radial distribution pattern across the annulus. At first chord length is assumed as half the length of the span as aspect ratio was assumed as 2; which gives an appropriate Reynolds number by equation:

$$Re = w_r . c/v$$

Where, v is the velocity of air at S.T.P.

Airfoil selection is primarily based on Reynolds number, thickness ratio, and chord length, maximum camber in chord percentage, lift and pressure coefficients. C4, NACA 4 digit and NACA 5 digit were compared and finally a combination of NACA 5digit nose droop with C4 profile called as F-series in literature has been selected for use in construction of blade.

A sample profile of the F-Series aerofoil was presented in below figure 4.

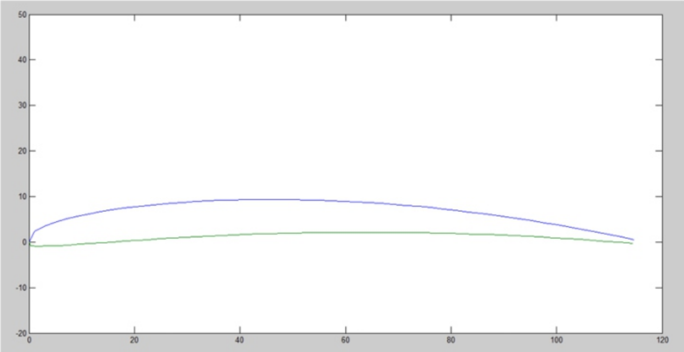

Fig. 4 Airfoil shape depicted using Matlab

III. CFD SIMULATION

ANSYS CFX has been used for CFD simulation of the product designed. To bring the simulation results closer to real-life operating conditions, to a CAD model at the inlet of the impeller a rig section which is long enough that the flow entering the impeller domain can be considered as a fully developed with the 3 Dpipe, and at the outlet where an ambient condition prevails another pipe with a length of 2 Dpipe was included. Its pictorial depiction was shown in below figure 5.

A. Boundary conditions

We need to define the velocity inlet as a boundary condition at the inlet section and pressure exit at the outlet section. After a steady state solution is obtained, the pressure difference is calculated by using the surface integral options of the fluent program. This option is more reliable and enhances a good control of volumetric flow.

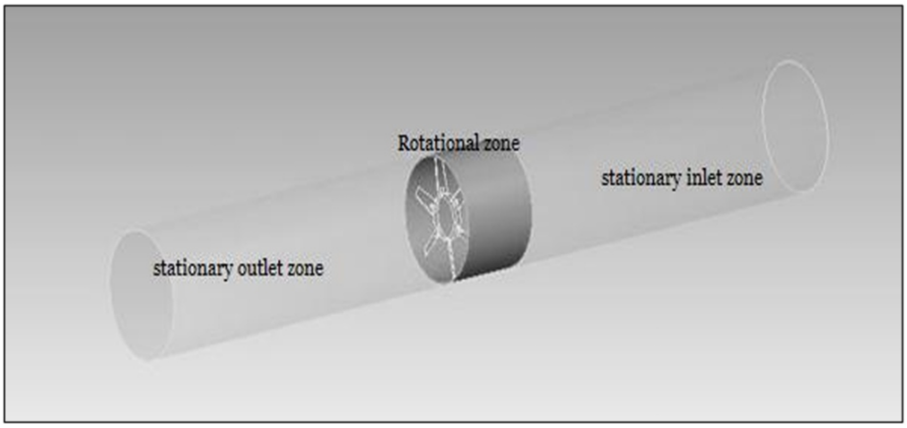

Fig. 5 CAD model of full system

The inlet boundary with specified velocity was applied to the rig domain, flow direction normal to the boundary condition and medium turbulence intensity (5%). A rotational speed of 1450 rpm was applied to the fan domain. The outlet boundary was applied to the ambient domain by specifying a 250C temperature with an air density of 1.07 kg /m3.

Since some part of the fluid zone is defined by a moving reference frame and some part of the fluid is stationary, grid interface panel is used to define the interactions. The turbulence model used in the solution is selected as RNG k-ε model. With reference to [18], has satisfactory results using the RNG k-ε turbulence model in designing of a reversible axial flow fan. This model is used for complex shear flows having rapid gradients, moderate swirl, vortices and local translations. Standard wall functions are used and the swirl dominated flow option is activated.

B. CFD RESULTS

Alongside with static pressure contours, velocity contours are also presented in figures 6 and 7. As the fan is designed according to the assumption of free vortex theory, which state no flow zone exists in radial direction.

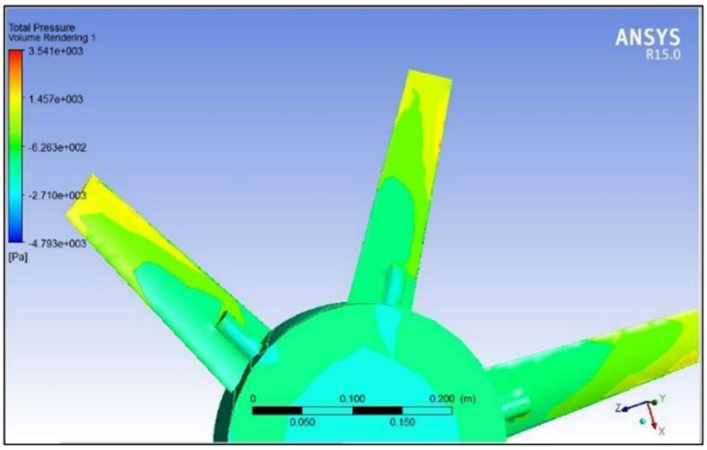

Fig. 6 Pressure contour at suction side

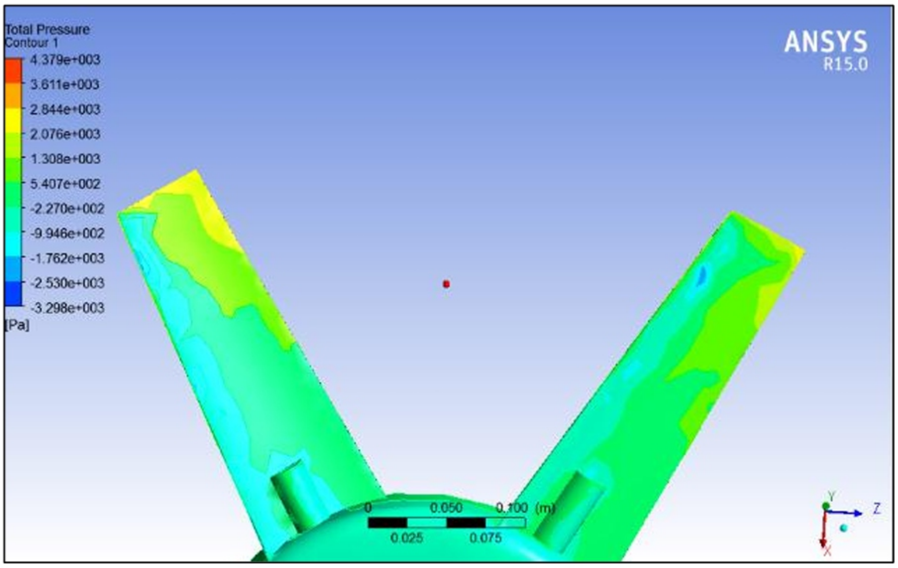

Fig 7 Pressure contour at pressure side

A typical CAD model of the airfoil and the flow domain around it was illustrated below in figure 8.

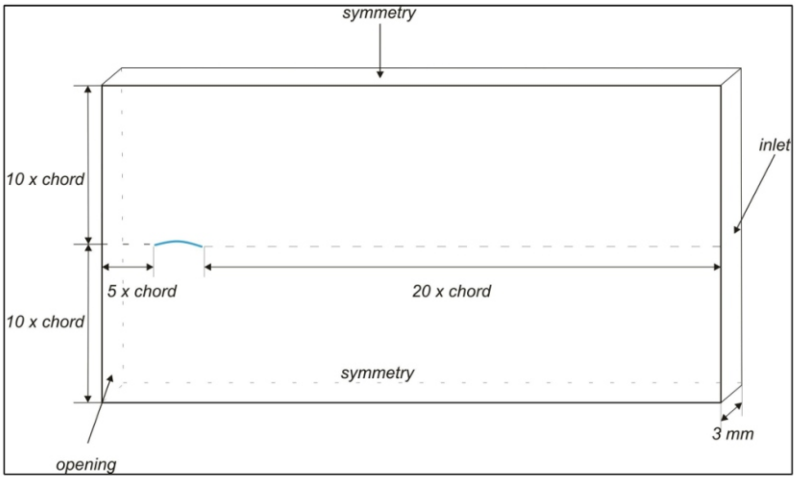

Fig. 8 Model of flow domain around an airfoil (adapted from [10])

Boundary conditions are key to play a simulation for an appropriate result that should be satisfactory. So, care has been taken while considering boundary conditions. At the inlet section, the specified flow velocity which is nothing but an axial velocity acting over a meridional section of a blade profile, which is calculated to be 16 m/s.

Outlet of the domain was open boundary, which is true with the case to have an ambient pressure. On to the lateral surfaces, symmetry boundary has been set, over to the top and bottom of the domain is also a symmetry boundary. As up on observation, after a height of the domain of 20 times the chord length from top to bottom, the difference in results between applying symmetry and / or opening boundary will sought to be negligible. The simulations were carried out for viscous flow with air as ideal gas. While coming to mesh properties, O-grid structured topology had been applied for the block corresponding to to the profile with a choice of tetrahedral mesh, which is a convenient option for better results.

As the case is up on static pressure variation with flow rate, a qualitative appreciation of pressure contours have been depicted in figure 9, which are helpful while identifying different sources of losses in the system; where the leading edge of the blade and the areas close to the tip section are critical due to tip clearance.

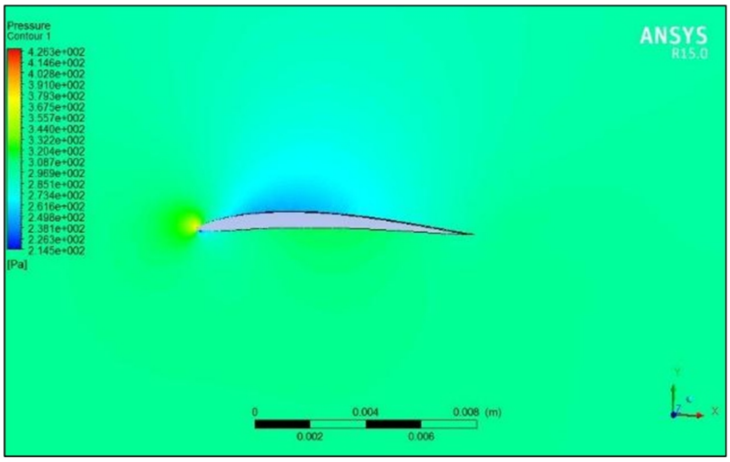

Fig. 9 Pressure contour of modified airfoil (f series)

IV. RESULTS AND ANALYSIS

Lift to drag ratio being relatively independent to coefficient of lift, the drag coefficients opted therein produces conservative estimates of the fan efficiency. This effect was observed and plotted in figure 10.

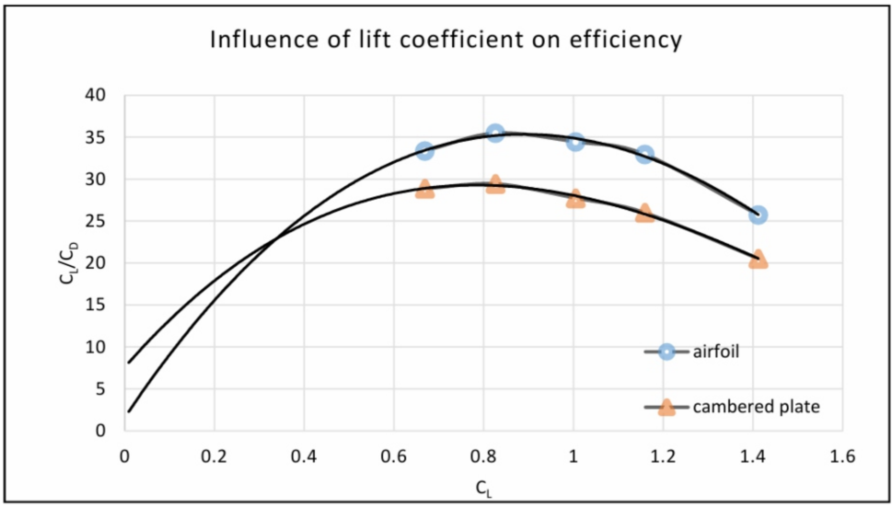

Fig. 10 Lift to drag ratios comparison w.r.t total to static efficiency

The rotor efficiency one way or the other depends mainly on the ratio [Cl\ (Cdp + Cds)]. This ratio is plotted in above figure as a function of Cl and Cd on the assumption that Cds is proportional to Cl 2. Hence design values of Cl approaching unity appear to give optimum performance when profile drag remains constant. But in practice, Cdp will increase moderately with Cl, so as an optimal value generally it is less than 0.8. Through optimal value of Cl efficiency losses of profile and secondary drag can be evaluated in the design process. For cambered plate blades, as observed, from the loss in efficiency will be up to 50 per cent greater than that of aerofoils generally used.

The below figure 11 presents the pitch to chord ratio across the radii for the rotor. The variation of the pitch to chord ratio is high in the rotor designed and as a result the blade has to be tapered. A tapered blade possesses a smaller chord as one moves from hub to tip.

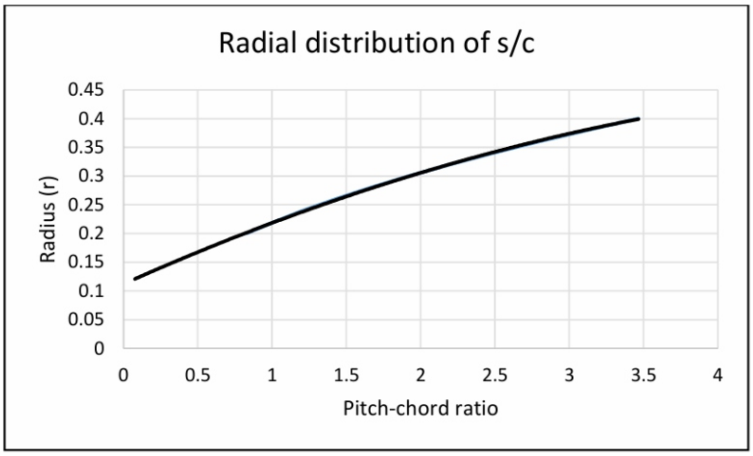

Fig. 11.a Radial distribution of pitch to chord ratio

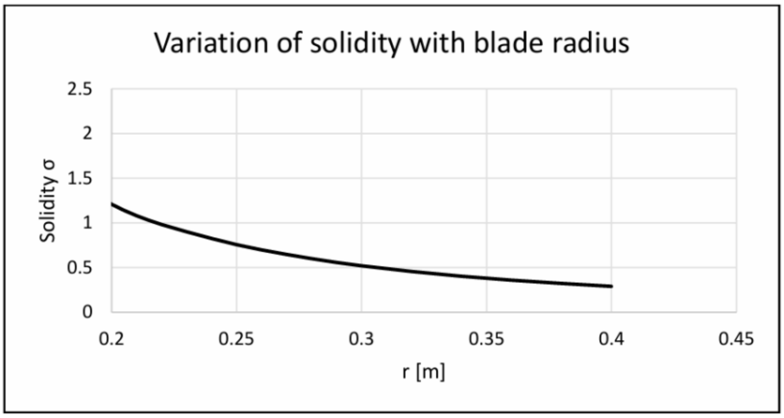

Fig. 11.b Variation of the solidity along the radius of the blade

The below figure 12 illustrates the relative velocities angles of the blade w.r.t radial distribution. The variation of the air angles (beta1, beta2) across the radii is in a good agreement with Wallis recommendations.

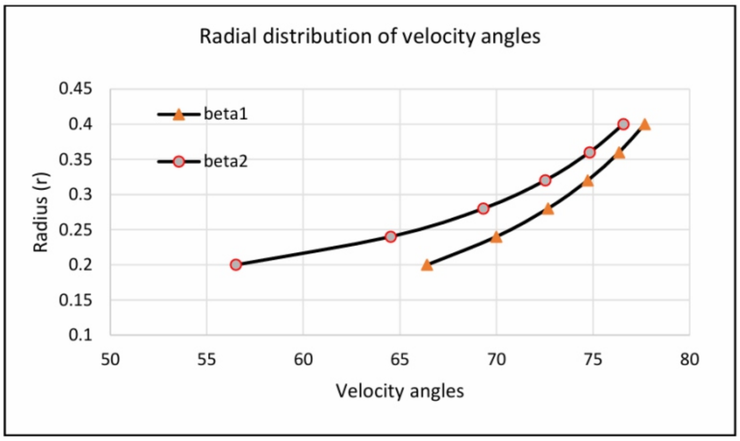

Fig. 12 Radial distribution of velocity angles

If in any case, the fan continues to operate outside of the stall region of its performance curve, air flow will continue to increase as if the chord angle increases from about 20° to 60°. As to the industrial data ought from industry, many existing fan systems are operating in unknown areas of their performance curve and a change in chord angle gives unpredictable results. Here in figure 13, the flow is increased rapidly as the chord angle is increased from approximately 40°.

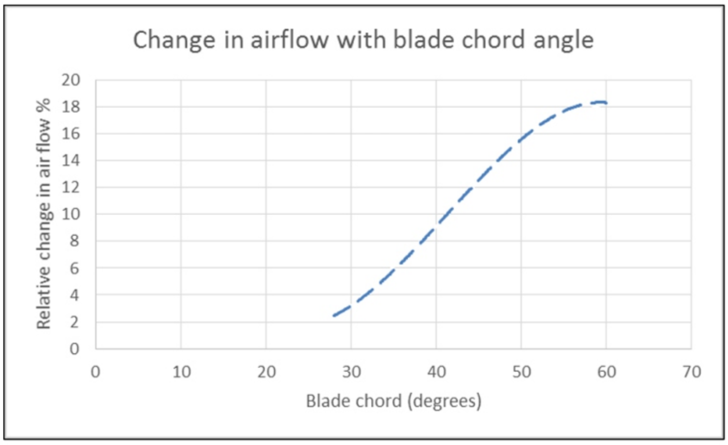

Fig. 13 Change of airflow with blade chord angle

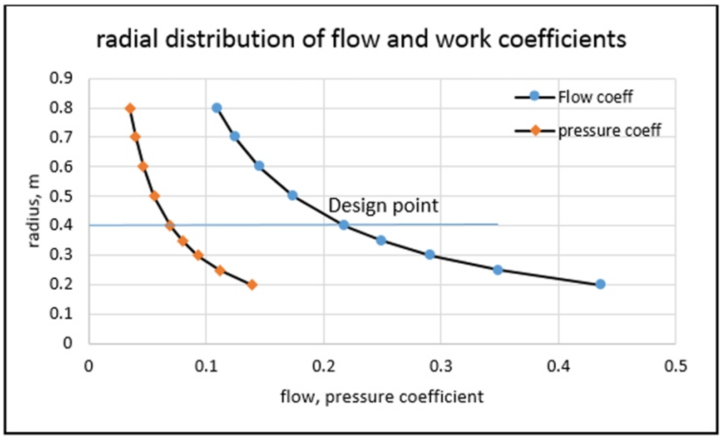

Fig. 14 Radial distribution of flow and work coefficients

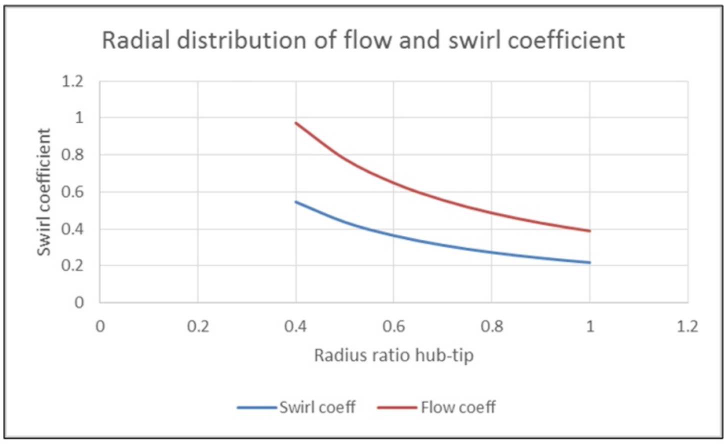

Fig. 15 Radial distribution of flow and swirl coefficient

The distribution of the flow and work coefficients across the radii has been plotted in above figure 15. Both values decrease as we move from hub to tip.

Radial distribution of flow and swirl coefficients has been presented here in figure 15.

Fan rotor design is mostly variable driven, which can be estimated as a function of the flow and swirl coefficients. In present work, these are extensively used in congruence with graphical representations, where the coordinates varies along y-axis and the flow coefficient. These graphs facilitates enough for design purposes of present work. These play key role in process of estimating efficiency. A series of iterative formulations have been in use for collection of data required to plot these graphs.

However, from the design perspective it is important to make sure about the proposed model that need to perform better according to the flow analysis, which needs performance analysis.

The fan design point can be defined as 300 Pascal of static pressure which relates to a total pressure of 361 Pascal with a volumetric flow rate of 5 m^3/s.
The efficiency is calculated by the equation below;

$$\eta_{hyd} = \frac{P_{total} \cdot Q}{T \cdot \omega}$$

Where the numerator is the fluid power and denominator is the shaft power. Table 2 presents the CFD results for 1450 rpm rotor and compared with design point.

The moment about the shaft axis is calculated to be 18.45 Nm as magnitude, which constitutes to get an efficiency of 63.18% of total hydraulic efficiency which is against 65% of design value raising to 2.8% of error in efficiency which is an acceptable one according to Lohner [20]. The hydraulic efficiency value is lower than the analytical value. It is mainly because of the cascade data for F series aerofoils are not sufficient. But 63.18% is still an acceptable and good value for axial flow fan about this size when compared to the 52% of total efficiency of the previous reference fan model.

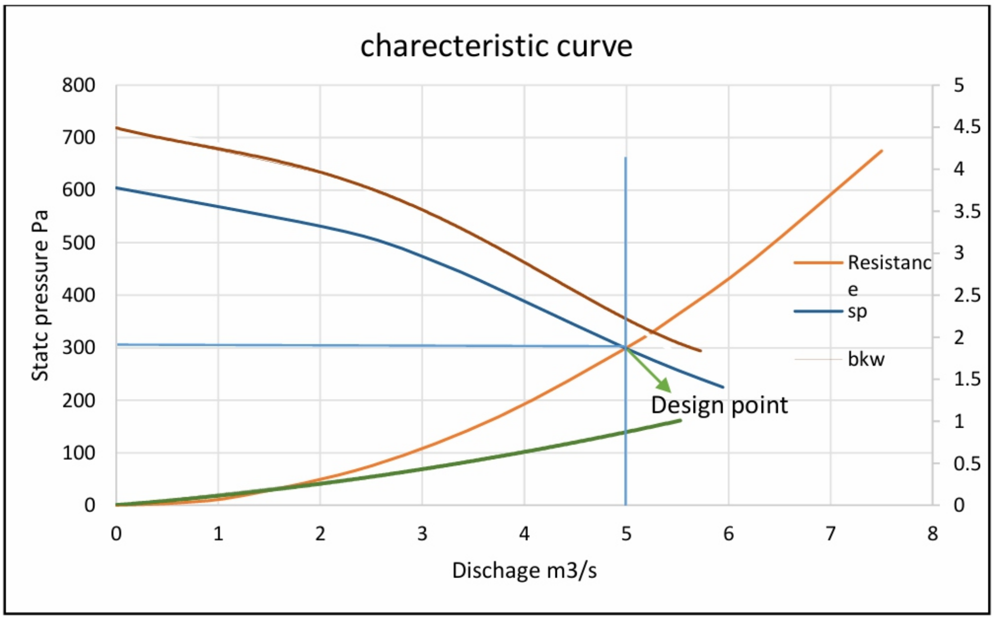

Fig. 16 Performance curve of present design

Table-2 Gauge total pressures of rotor

	Q (m^3/s)	P_{total} (Pascal)	T (Nm)
CFD	5	354	18.45
Design	5	361	17.937

The designed axial fan will be operated at open condition for kiln-shell cooling which causes force convection to the wall of kiln-shell, which when compared with other applications, the operating range can deliberated to be a very narrow case.

The results of simulation are presented in graphical form in Figure 17. Static pressure rise and efficiency values are plotted with respect to the volumetric flow rate. As described previously, the operating range of the fan is very narrow, so the calculations do not cover fan stall regions, closed valve regions and zero pressure loss regions.

$$error = \frac{|P_{CFD} - P_{analytical}|}{P_{analytical}} \, .100$$

An error can be defined as the difference of pressure rise between analytical result and computational result as a percentage of the analytical result. The error is calculated as 1.19 %.

This simulation is used as a validation tool for the design and congruency met by the simulation result with the analytical value is good enough to consider for practical application.

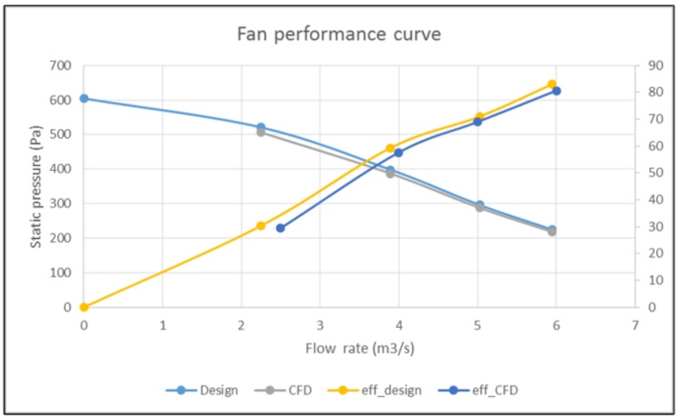

Fig. 17 Fan performance curves

V. CONCLUSIONS

The total pressure rise through the rotor is in agreement with the analytical design. However, total to static efficiency is computed to be 71% as against 67% of the existing fan.

The pressure contours of the CFD results are also in agreement with free vortex flow.

The pressure contours are aligned from hub to tip in a parallel way. In addition, when the operating condition is different from the design point the pressure contours deteriorates.
Cooling is an important factor and it must be taken into consideration for Kiln shells. Cooling with air exchange may not be an option, if the environment temperature is high. Cooling option through corner vanes or diffusers can be studied for future work. By using the design approach model presented in this paper, not only for kiln-shell cooling but also can be useful for scientific wind tunnels in subsonic regimes or automobile fans, which can be designed and built. The design in this manuscript is for given site conditions, if the location is different, the duct or tube axial fan design must be optimized for these conditions.

The terminal velocity, which derives the design, changes nonlinearly with altitude. This situation must be taken into account during design. CFD is used to analyse the total pressure increase and static pressure rise across the rotor of the fan. Since the operating region is far from the fan stall point, flow separation or instabilities had not been investigated. Although CFD is a powerful tool for flow analysis, it must be backed up by experimental data which could be a future scope of this work. In brief, with / of design approach has been presented in figure 18; which later CFD simulation follows with a numerical analysis and has been presented with graphical and contour plots as results in above sections.

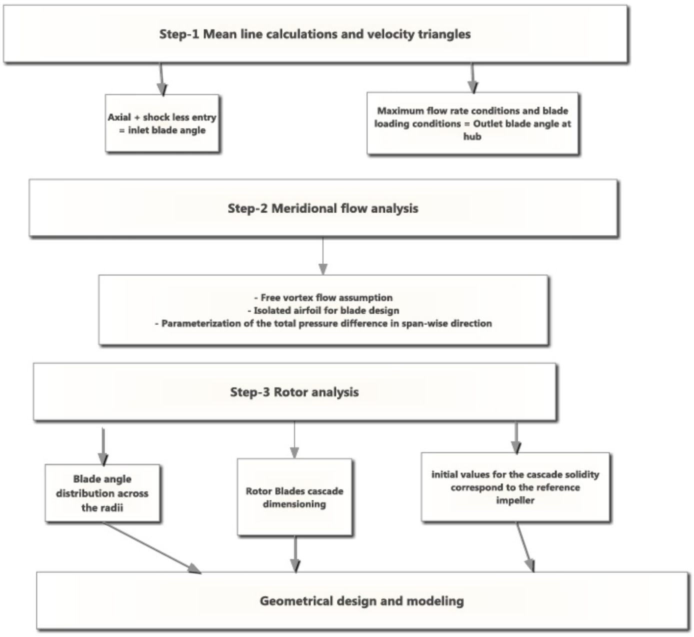

Fig. 18 Simplified flow chart of the design process

REFERENCES

[1] "Fans", Bruno Eck, Pergamon Press. 55

[2] "Fans & Ventilation - A Practical Guide"; W T W (Bill) Cory, Elsevier publishers, 2005.

[3] "Axial flow fans, design and practice", R.A.Wallis, 1961.

[4] "Fan Handbook", Franck P Bleier, 1998.

[5] "The fan including the theory and practice of centrifugal and axial fans", Charles H. Innes.

[6] "An Engineering Approach to Blade Designs for Low to Medium Pressure Rise Rotor-Only Axial Fans", R.A.Wallis et.al, CSIRO Experimental Thermal and Fluid Science, 1993.

[7] "Turbomachinery performance analysis", R.I Lewis, 1996.

[8] "Developments in Turbomachinery Flow" by Nader Montazerin et.al.

[9] "A theoretical derivation of the Cordier diagram for turbomachines"; Epple et.al, Journal of Mechanical Engineering Science, 2011.

[10] "Axial fan design: modern layout and design strategy for fan performance optimization" by Maria Pascu

[11] "The Design and Performance of an Axial-Flow Fan"; Lionel s. Marks et.al, AER-53-13, transactions of the american society of mechanical engineers, 1934.

[12] "Analytical Models for Axial Fan Performance Rating"; Daniel Khalitov, Ganesh. R; AMCA Engineering Conf, Las Vegas, NV, 2008

[13] "A Comparison of Two Methods for Predicting the Potential Flow around Arbitrary Airfoils in

Cascade"; D. Pollurd and J. Wordsworth, 1963.

[14] "Fluid machinery: application, selection, and design"; Gerhart and Wright, 2nd edition, 2009.

[15] "Design and Analysis of Propeller Blade Geometry using the PDE Method" by Christopher Wojciech Dekanski, Phd thesis.

[16] "A Parametric Blade Design System"; Hans Heukenkamp lecture notes

[17] "Airfoil Aerodynamics Using Panel Methods" by Richard L. Fearn

[18] "Centrifugal and axial fan applications and design criteria" by I.Howitt

[19] "Principles of turbomachinery"; R.K.Turton, 2nd edition, 1995.

[20] "Applied computational fluid dynamics techniques"; Rainald Löhner, 6th edition, 2008.

[21] AMCA standard 210.

[22] IS 3588 & 4894.

[23] ANSYS CFX Reference Guide.

Instructions for Authors

Essentials for Publishing in this Journal

1 Submitted articles should not have been previously published or be currently under consideration for publication elsewhere.

2 Conference papers may only be submitted if the paper has been completely re-written (taken to mean more than 50%) and the author has cleared any necessary permission with the copyright owner if it has been previously copyrighted.

3 All our articles are refereed through a double-blind process.

4 All authors must declare they have read and agreed to the content of the submitted article and must sign a declaration correspond to the originality of the article.

Submission Process

All articles for this journal must be submitted using our online submissions system. http://enrichedpub.com/ . Please use the Submit Your Article link in the Author Service area.

Manuscript Guidelines

The instructions to authors about the article preparation for publication in the Manuscripts are submitted online, through the e-Ur (Electronic editing) system, developed by **Enriched Publications Pvt. Ltd**. The article should contain the abstract with keywords, introduction, body, conclusion, references and the summary in English language (without heading and subheading enumeration). The article length should not exceed 16 pages of A4 paper format.

Title

The title should be informative. It is in both Journal's and author's best interest to use terms suitable. For indexing and word search. If there are no such terms in the title, the author is strongly advised to add a subtitle. The title should be given in English as well. The titles precede the abstract and the summary in an appropriate language.

Letterhead Title

The letterhead title is given at a top of each page for easier identification of article copies in an Electronic form in particular. It contains the author's surname and first name initial .article title, journal title and collation (year, volume, and issue, first and last page). The journal and article titles can be given in a shortened form.

Author's Name

Full name(s) of author(s) should be used. It is advisable to give the middle initial. Names are given in their original form.

Contact Details

The postal address or the e-mail address of the author (usually of the first one if there are more Authors) is given in the footnote at the bottom of the first page.

Type of Articles

Classification of articles is a duty of the editorial staff and is of special importance. Referees and the members of the editorial staff, or section editors, can propose a category, but the editor-in-chief has the sole responsibility for their classification. Journal articles are classified as follows:

Scientific articles:

1. Original scientific paper (giving the previously unpublished results of the author's own research based on management methods).

2. Survey paper (giving an original, detailed and critical view of a research problem or an area to which the author has made a contribution visible through his self-citation);

3. Short or preliminary communication (original management paper of full format but of a smaller extent or of a preliminary character);

4. Scientific critique or forum (discussion on a particular scientific topic, based exclusively on management argumentation) and commentaries. Exceptionally, in particular areas, a scientific paper in the Journal can be in a form of a monograph or a critical edition of scientific data (historical, archival, lexicographic, bibliographic, data survey, etc.) which were unknown or hardly accessible for scientific research.

Professional articles:

1. Professional paper (contribution offering experience useful for improvement of professional practice but not necessarily based on scientific methods);
2. Informative contribution (editorial, commentary, etc.);
3. Review (of a book, software, case study, scientific event, etc.)

Language

The article should be in English. The grammar and style of the article should be of good quality. The systematized text should be without abbreviations (except standard ones). All measurements must be in SI units. The sequence of formulae is denoted in Arabic numerals in parentheses on the right-hand side.

Abstract and Summary

An abstract is a concise informative presentation of the article content for fast and accurate Evaluation of its relevance. It is both in the Editorial Office's and the author's best interest for an abstract to contain terms often used for indexing and article search. The abstract describes the purpose of the study and the methods, outlines the findings and state the conclusions. A 100- to 250- Word abstract should be placed between the title and the keywords with the body text to follow. Besides an abstract are advised to have a summary in English, at the end of the article, after the Reference list. The summary should be structured and long up to 1/10 of the article length (it is more extensive than the abstract).

Keywords

Keywords are terms or phrases showing adequately the article content for indexing and search purposes. They should be allocated heaving in mind widely accepted international sources (index, dictionary or thesaurus), such as the Web of Science keyword list for science in general. The higher their usage frequency is the better. Up to 10 keywords immediately follow the abstract and the summary, in respective languages.

Acknowledgements

The name and the number of the project or programmed within which the article was realized is given in a separate note at the bottom of the first page together with the name of the institution which financially supported the project or programmed.

Tables and Illustrations

All the captions should be in the original language as well as in English, together with the texts in illustrations if possible. Tables are typed in the same style as the text and are denoted by numerals at the top. Photographs and drawings, placed appropriately in the text, should be clear, precise and suitable for reproduction. Drawings should be created in Word or Corel.

Citation in the Text

Citation in the text must be uniform. When citing references in the text, use the reference number set in square brackets from the Reference list at the end of the article.

Footnotes

Footnotes are given at the bottom of the page with the text they refer to. They can contain less relevant details, additional explanations or used sources (e.g. scientific material, manuals). They cannot replace the cited literature.

The article should be accompanied with a cover letter with the information about the author(s): surname, middle initial, first name, and citizen personal number, rank, title, e-mail address, and affiliation address, home address including municipality, phone number in the office and at home (or a mobile phone number). The cover letter should state the type of the article and tell which illustrations are original and which are not.